Investigating the stochastic dispersion of 2D engineered frame structures under symmetry of variability

Luiz H. M. S. Ribeiro[1,*], Vinícius F. Dal Poggetto[2], Danilo Beli[3], Adriano T. Fabro[4], José R. F. Arruda[1]

Abstract

Additive manufacturing has enabled the construction of increasingly complex mechanical structures. However, the variability of mechanical properties may be higher than that of conventionally manufactured structures. Typically, the computational cost of the numerical modeling of such structures considerably increases when variability is considered. In deterministic analyses of periodic structures, the dispersion diagrams obtained for the first Brillouin zone (FBZ) can be used to predict attenuation bands for any direction of propagation. This can be further simplified considering only the contour of the irreducible Brillouin zone (IBZ) if the unit cell presents symmetries. The objective of the current investigation is to present evidence that, similarly to what occurs in deterministic cases, the stochastic results obtained by scanning only the IBZ contour of the proposed two-dimensional unit cell under 4-fold rotational symmetry of statistical variability coincides with statistical results obtained scanning the FBZ. This is not a direct result, because each individual unit cell sample is asymmetric. We show that, under symmetry of variability statistics, the stochastic results computed for supercells and for finite metastructures consisting of a finite number of cells also coincide with the results for the IBZ contour of the unit cell.

*Corresponding author
Email address: luiz.marra@outlook.com (Luiz H. M. S. Ribeiro)
[1]University of Campinas, School of Mechanical Engineering, Campinas, Brazil, 13083-860.
[2]Department of Civil, Environmental and Mechanical Engineering, University of Trento, Trento, Italy, 38123.
[3]University of São Paulo, São Carlos School of Engineering, Department of Aeronautical Engineering, São Carlos, Brazil, 13566-590.
[4]University of Brasilia, Department of Mechanical Engineering Brasilia, 70910-900, Brazil.

This result is important, as it dramatically reduces the computation cost of the stochastic analysis of such structures.

Keywords: Mechanical variability, additive manufacturing, Bayes' factor, periodic structure, robust band gap.

1. Introduction

Mechanical vibrations may be detrimental in structural applications [1, 2, 3, 4]. The design of supporting phononic or metamaterial structures that isolate vibrations using wave band gaps, i.e., frequency bands where there is no wave propagation [2, 5, 6], is a current topic of research [7, 8]. In addition, additive manufacturing has made the (meta)material design possible through a wide variety of lightweight complex geometries, without the loss of effective mechanical stiffness [1].

In this context, investigating two-dimensional lattices composed by 1D waveguides is interesting because they are halfway between one-dimensional simple models and more complex three-dimensional models, allowing the investigation of directionality without exceedingly complex analytical formulations [9, 10] and computational burden [11, 12]. They may also have important applications in machine design [11, 13, 14, 15]. Some examples of two-dimensional metastructures are plane frame structures with resonators [4], plates with polynomial decrement of their thickness in specific regions (acoustic black holes) [7, 8], and periodic inclusions [12].

Recent studies have reported cases where the variability of the mechanical properties of waveguides obtained by additive manufacturing substantially influenced the observed dynamic responses [1], thus showing the necessity of quantifying the uncertainties related to this variability [5, 3, 16, 17]. Statistical methods have been used to estimate and to infer about the statistical distribution of the model parameters. The inferred distributions are used to obtain the stochastic response using the deterministic model [1, 16, 18, 19, 20]. It is known that the greater the sample size, the better the inference, but the greater the experimental effort [21]. However, using the correct prior information and Bayesian statistics, the final result can present better precision at a smaller experimental effort [22]. The correct application of the Bayesian approach usually yields less biased estimates and improves precision and accuracy [19, 23].

Statistical methods have been used for uncertainty quantification in many fields, including structural dynamics [1, 18, 24]. In statistics, there are two main approaches: frequentist and Bayesian [25, 26]. Bayesian statistics uses prior information that is available before the experiments [22]. In previous studies, a Bayesian estimator, which used Prony's method to estimate the wavenumbers from experimental data, was considered [27]. It has also been shown that it is possible to use this highly precise inference to generate stochastic fields that simulate spatial variability of mechanical properties in periodic structures using statistical tools such as Karhunen–Loève (KL) expansion and the expansion optimal linear estimator (EOLE) [10, 20].

Recent investigations focused on the robustness of band gaps of two- and three-dimensional structures. In some studies, the robustness of the band gap is considered in terms of the band gap width and/or location [28, 29, 30, 31, 32, 33], while, in others, in terms of defects [34, 35]. Some studies address the variability related to the dimensions of local resonators [36, 37, 38]. Also, the variability of all geometric dimensions of a three-dimensional PC is considered when dealing with band gap robustness [16]. Sensitivity analysis was used to identify the random variable that most influences the band gap [39]. Recently, a study that considered the mechanical properties as spatially correlated random variables was also reported [40, 41, 42, 43]. Another recent study on uncertainty in the scattering matrix of mechanical joints reports symmetric average scattering under symmetry of variability [44]. Two main concerns observed in the literature are dealt with in the current study: (i) the lack of computationally efficient methodologies for analyzing attenuation bands in periodic structures (metamaterials or PCs) under variability; and (ii) the lack of investigations of the relationship between the dispersion diagrams computed on the IBZ or FBZ contours for the unit cells, on the IBZ of supercells, and the forced responses of metastructures (finite metamaterials or PCs) with spatial variability.

The deterministic approach is presented in detail in the Appendices and consists of obtaining the minimum of the imaginary part (minimum attenuation) of all the computed wavenumbers using the model of a frame cell based on the Spectral Element Method (SEM). The stochastic methodology combines the computed attenuation bands with EOLE to model the spatial variability and the Monte Carlo (MC) method. Similarly to the Bayes' factor, a ratio of chances is used to infer the stochastic results.

The objective of the current study is to show evidence that, for 2D periodic structures with rotational symmetry of variability, it is possible to infer the stochastic wave attenuation of metastructures by analyzing only the IBZ of its unit cell, as it occurs in the deterministic case. By symmetry of variability, we mean that the same description of the spatial variability of the frame elements, either by random variables or random fields with specified correlation function and correlation length, is used for the frame elements of the unit cell. We call this a rotational symmetry of variability. The presented results for a 4-fold rotational symmetry of variability are novel. This original result is important for simulating the stochastic of periodic frame structures because of the dramatic computational cost reduction it allows. The stochastic wave attenuation bands on the IBZ contour coincide with the stochastic wave attenuation bands on the FBZ, with the stochastic wave attenuation on the IBZ of a supercell, and with stochastic forced responses computed for finite metastructures. The results are computed for three different two-dimensional frame cells modeled using Euler-Bernoulli (EB) and Timoshenko (T) beam theories. The presented stochastic wave propagation properties are not as direct as they are for the deterministic cases, because each unit cell obtained as a sample of the stochastic field does not present 4-fold deterministic rotational symmetry of mechanical properties nor periodicity over the metastructure. However, when looking at the spatial distribution of variability, there is 4-fold rotational symmetry over the unit cell and periodicity over the metastructure.

In Section 2, we present the SEM modeling of a frame element and the deterministic results. The two-dimensional modeling and the strategies for sampling the IBZ and FBZ contours are presented in Section 3. The methodology for modeling finite metastructure and for simulating the spatial variability are presented in Section 4. In Section 4, results show that, under symmetry of variability, stochastic results for the IBZ are equivalent to results for the FBZ for different two-dimensional cells and for different types of variability. In addition, it is shown that the dispersion diagrams computed for the stochastic two-dimensional unit frame cell on the IBZ contour also coincide with the IBZ results for the supercell and with the forced responses for a metastructure built up with the frame cell. Section 5 presents the concluding remarks concerning the evidence about the equivalence of the results for the IBZ and the FBZ of a two-dimensional cell, results for the IBZ of the supercell, and forced responses of a metastructure. This is valid for stochastic cases under 4-fold rotational symmetry of the variability.

2. Obtaining the wavenumber from a two-dimensional frame cell

The dynamic stiffness matrix of a structural frame element ($\boldsymbol{D}_f(\omega)$) can be obtained via the SEM, which is reviewed in Appendix A for the elementary rod, the EB and the T beam theories. If the modeled frame element is not homogeneous, it can be modeled in a piece-wise form and the dynamic condensation procedure can be applied to reduce the dimensionality of the problem (see details in Appendix B). Using the assumption of uncoupled flexural and longitudinal behavior (see Fig. 1b), the plane frame element can be obtained by assembling the rod (D_r) and beam matrices (D_b), as presented in Eq. (1) [45].

$$\boldsymbol{D}_f(\omega) = \begin{bmatrix} D_{r,11} & 0 & 0 & D_{r,12} & 0 & 0 \\ 0 & D_{b,11} & D_{b,12} & 0 & D_{b,13} & D_{b,14} \\ 0 & D_{b,12} & D_{b,22} & 0 & D_{b,23} & D_{b,24} \\ D_{r,12} & 0 & 0 & D_{r,11} & 0 & 0 \\ 0 & D_{b,13} & D_{b,23} & 0 & D_{b,11} & D_{b,34} \\ 0 & D_{b,14} & D_{b,24} & 0 & D_{b,34} & D_{b,22} \end{bmatrix}, \tag{1}$$

where the subscript ij denotes the element at the i-th row and j-th column of the considered matrix.

After a frame element is modeled and condensed, a built-up structure (metastructure) can be assembled into the global stiffness matrix ($\boldsymbol{D}_g(\omega)$) similarly as in the finite element (FE) method [46, 47]. The matrix $\boldsymbol{D}_g(\omega)$ relates all external displacements and forces of all assembled frames in matrix form for a given frequency ω [48, 49, 50]

$$\boldsymbol{D}_g(\omega)\mathbf{u} = \mathbf{F}, \tag{2}$$

where vector $\mathbf{u}$ represents the nodal displacements and/or rotations, vector $\mathbf{F}$ represents the external nodal forces and/or moments, and matrix $\boldsymbol{D}_g(\omega)$ is the dynamic stiffness matrix.

The two-dimensional unit cell of the Lieb lattice (Fig. 1a) [48, 49, 50] modeled via its global stiffness matrix (Eq. (2)) using four frame elements. Appendix C presents a procedure of assembling $\boldsymbol{D}_g(\omega)$ and the condensation of nodes $\mathbf{q}_4$ and $\mathbf{q}_5$. After $\mathbf{q}_4$ and $\mathbf{q}_5$ are condensed, the dynamic equations of motion may be expressed using the condensed global stiffness matrix $\boldsymbol{D}_c(\omega)$ as

$$\begin{bmatrix} \boldsymbol{D}_{11} & \boldsymbol{D}_{12} & \boldsymbol{D}_{13} \\ \boldsymbol{D}_{21} & \boldsymbol{D}_{22} & \boldsymbol{D}_{23} \\ \boldsymbol{D}_{31} & \boldsymbol{D}_{32} & \boldsymbol{D}_{33} \end{bmatrix} \begin{Bmatrix} \boldsymbol{u}_1 \\ \boldsymbol{u}_2 \\ \boldsymbol{u}_3 \end{Bmatrix} = \begin{Bmatrix} \boldsymbol{F}_1 \\ \boldsymbol{F}_2 \\ \boldsymbol{F}_3 \end{Bmatrix} \quad \rightarrow \quad \boldsymbol{D}_c(\omega)\mathbf{u}_c = \mathbf{F}_c, \tag{3}$$

where the vectors $\mathbf{u}_c$ and $\mathbf{F}_c$ are related to the nodes $\mathbf{q}_1$, $\mathbf{q}_2$, and $\mathbf{q}_3$.

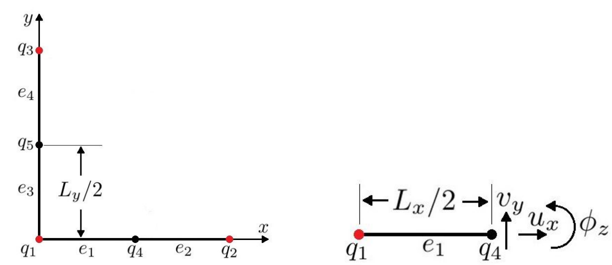

(a) (b)

Figure 1: (a) The proposed two-dimensional frame cell, made of four plane frame elements (e_1, e_2, e_3, and e_4). Red nodes (q_1, q_2, and q_3) are kept and the black nodes are condensed (q_4 and q_5). (b) Representation of the longitudinal (u_x), flexural (v_y) and torsional (ϕ_z) degrees of freedom (DOFs) for the frame element e_1.

The Bloch-Floquet periodic conditions [14, 51] can be applied to $\boldsymbol{D}_c(\omega)$ in order to compute the dispersion relation of the Lieb unit cell. A relatively low computational cost, when compared with the $\omega(k)$ approach using an FE model, is required for solving a $k(\omega)$ problem using SEM. This can be explained by the significant reduction in the dynamic matrix dimensions allowed by SEM, especially at higher frequencies. Although the considered $k(\omega)$ method does not take advantage of the symmetry and sparsity of FE matrices when using an $\omega(k)$ method, the resulting reduced dimensions allows an efficient computational cost when finding the roots of the polynomial in Eq. 7 for a variable ω using the companion matrix. In addition, it results in an analytical solution in the frequency domain [53]. This methodology is briefly presented in the following paragraphs and in Appendix D, because a non-conventional procedure is proposed to improve the ill-conditioning inherent to this problem.

Using the Bloch-Floquet theorem [54, 55], and defining the propagation constant in the x direction as λ_x and the propagation constant in the y direction as λ_y, it is possible to define the relationship between the displacements of the nodes at different unit cell boundaries by Eq. (4).

$$\begin{Bmatrix} \mathbf{q}_1 & \mathbf{q}_2 & \mathbf{q}_3 \end{Bmatrix}^T = \begin{bmatrix} \mathbf{I}_n & \mathbf{I}_n\lambda_x & \mathbf{I}_n\lambda_y \end{bmatrix}^T \mathbf{q}_1 \qquad \rightarrow \qquad \boldsymbol{q} = \boldsymbol{\Lambda}_R\, \boldsymbol{q}_1, \tag{4}$$

where $\boldsymbol{\Lambda}_R$ can be defined as the transformation matrix that relates $\mathbf{q}_1$, $\mathbf{q}_2$, and

$\mathbf{q}_3$ to $\mathbf{q}_1$.

Matrix $\mathbf{\Lambda}_L$, which assumes equilibrium of nodal forces, can be obtained using

$$\boldsymbol{F}_1 + \boldsymbol{F}_2\lambda_x^{-1} + \boldsymbol{F}_3\lambda_y^{-1} = \mathbf{0}, \tag{5}$$

yielding

$$\begin{bmatrix}\mathbf{I}_n & \mathbf{I}_n\lambda_x^{-1} & \mathbf{I}_n\lambda_y^{-1}\end{bmatrix}\begin{Bmatrix}\boldsymbol{F}_1 & \boldsymbol{F}_2 & \boldsymbol{F}_3\end{Bmatrix}^T = \mathbf{\Lambda}_L\boldsymbol{F} = \mathbf{0}. \tag{6}$$

Now, substituting Eq. (4) in the term $\boldsymbol{q}$ of Eq. (2), and premultiplying both sides by $\mathbf{\Lambda}_L$ one obtains

$$\mathbf{\Lambda}_L\boldsymbol{D}_c(\omega)\mathbf{\Lambda}_R\mathbf{q}_1 = \mathbf{0}. \tag{7}$$

The companion matrix can be used to solve Eq. (7) while maintaining the polynomial ordinary (see Appendix D). This procedure makes it possible to obtain the dispersion diagram for infinite number, but not continuous, values of θ in a substantive lower computational cost. An alternative method, which could also have been used to compute the wavenumbers in a numerically efficient way [57] is the shift-cell method [56]. The proposed procedure combined with the SEM modeling is of utmost importance when computing the stochastic response, which needs multiple simulations. A methodology to improve the matrix conditioning is presented in Appendix E and is illustrated by deterministic results presented in Appendix F and Appendix G.

A wavenumber with a non-negligible imaginary part is an evidence of evanescent behavior [58, 59]. A frequency band where all the waves are evanescent is here named attenuation band. If the wavenumber is complex, the real part is given by the number of radians per unit distance while the imaginary part gives an exponential decay, or attenuation, as the wave propagates [60]. The Bloch-Floquet theorem [54, 55], for a periodic waveguide, implies that the wavenumber consists of real and imaginary components. By considering an one-dimensional structure for the sake of simplicity, the wave propagating to the right-side of the waveguide is given by Ae^{-ikx}, where A is the wave amplitude, k is the complex wavenumber, x is the position along the waveguide and i is the imaginary unit number. Consequently, inspecting the previously mentioned mathematical expression, the percentage of attenuation per length due to the evanescent part of the wavenumber ($\mathrm{Im}(k)$), which has the dimension of m^{-1}, can be calculated [59]. The attenuation per meter can be given by

$$\delta_m = 100(1 - e^{-\mathrm{Im}(k)}). \tag{8}$$

It is a common procedure to calculate kL instead of k. Thus, the percentage of attenuation per cell length is given by

$$\delta_c = 100\left(1 - \left(e^{-\mathrm{Im}(kL)}\right)\right). \tag{9}$$

Bragg-type band gaps are characterized by a real part of the normalized wavenumber kL in the Bragg limits (0 and π) and a non-zero imaginary part [61]. However, in complex structures, the interpretation of the wave attenuation phenomenon is not as straightforward as the Bragg scattering band gap. Frequency bands where attenuation happens for all waves are called full band gaps. Furthermore, for two- or three-dimensional waveguides, if this also happens for all wave propagation directions, it may be considered as a full and complete band gap [20]. To characterize such bands, values of δ_c greater than a predefined threshold value for all waves are considered [10].

3. Deterministic results for the periodic structure

In this section, some deterministic results are presented. A two-dimensional frame cell with a circular radius (r) and length (L) (Fig. 2a) is proposed using four one-dimensional unit cell forming a Lieb lattice (Fig. 2b) and assessed considering the EB beam theory. The mechanical and geometric characteristics of segments f_1 (nylon) and f_2 (aluminum) are defined as $\mathrm{E}_1 = 2$ GPa, $\rho_1 = 1200$ kg/m^3, $\mathrm{L}_1 = 60$ mm, $\mathrm{r}_1 = 2.5$ mm, $\mathrm{E}_2 = 70$ GPa, $\rho_2 = 2700$ kg/m^3, $\mathrm{L}_2 = 60$ mm, $\mathrm{r}_2 = 4$ mm. It is possible to verify by inspecting the deterministic physical modes (see Appendix E) at Fig. 3 that there are mainly 7 full attenuation band for $\theta = 45°$: 2.25-4.25 kHz; 4.60-6.35 kHz; 7.05-7.98 kHz; 9.30-9.53 kHz; 11.43-14.38 kHz; 14.82-19.40 kHz; the last band starts at 23.8 kHz.

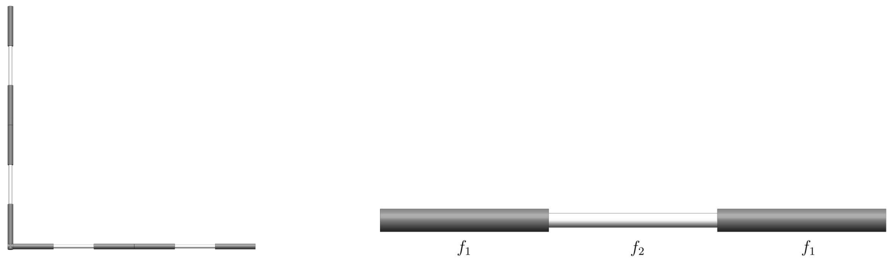

(a) (b)

Figure 2: (a) The first proposed Lieb unit cell made of four frame elements modeled via elementary rod and EB beam theories. (b) The defined symmetric frame element of three segments: nylon in the extremities and aluminum in the middle.

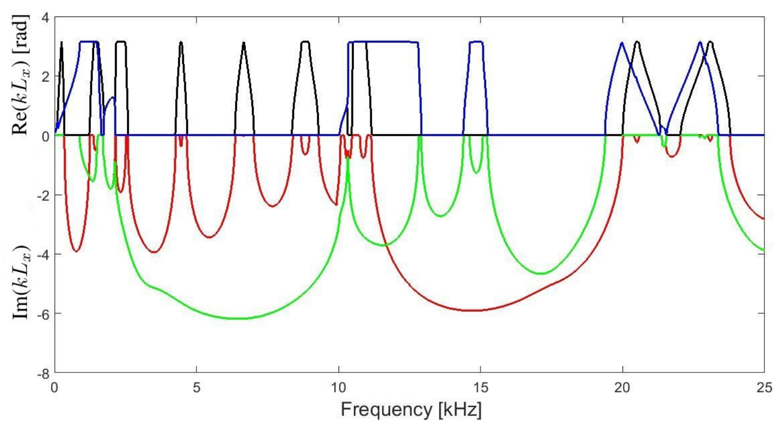

Figure 3: Real (blue and black) and imaginary (red and green) parts of the physical wave modes of the unit cell for $\theta = 45°$.

More complex structures can present richer dispersion diagrams. In addition, coupled systems can also present dispersion diagrams substantially different from uncoupled structures [62]. It is possible to notice from Fig. 3 four wide and full attenuation bands (2.25-4.25 kHz; 4.60-6.35 kHz; 11.43-14.38 kHz; 14.82-19.40 kHz). The causes of such attenuation bands are not as simple as for the one-dimensional periodic system. For instance, the causes of attenuation can be isolated or combined phenomenon: Bragg scattering [5], local resonance, wave veering, and locking effects [62].

Given the complexity of the dispersion diagrams, it is impracticable to analyze the causes of the wave attenuation for the hundreds of stochastic responses. Therefore, the minimum value of the magnitude of the imaginary part of the normalized wavenumber ($\min(|\ \mathrm{Im}(kL)\ |)$) is used to observe the attenuation bands. If their value is greater than zero, it indicates there will be attenuation of all waves while traveling along the structure [63], even in the absence of structural damping. In practice, there may exist frequency ranges where, although there is no substantial wave attenuation, the computed ($\min(|\ \mathrm{Im}(kL)\ |)$) can be slightly greater than zero. For this reason, a minimum threshold value δ_k is considered to detect an attenuation at a given frequency, i.e., ($\min(|\ \mathrm{Im}(kL)\ |)) > \delta_k$. In the present study, two gray color patches were created for $\delta_k \approx 0.2$ and $\delta_k \approx 0.92$. Those values correspond to an attenuation of approximately at least 20% ($\delta_c \geq 20\%$) and 60% ($\delta_c \geq 60\%$) in all directions per cell length, respectively.

3.1. First Brillouin zone and irreducible Brillouin zone

The FBZ represents the dispersion relations for all possible propagation directions of a wave propagating in a periodic structure [64].For two-dimensional propagation, it is represented by a square for the Lieb unit cell (see the dashed line in Fig. 4a). If the two-dimensional structure presents symmetry, the symmetry will be manifested in the reciprocal space, and hence, it is not necessary to scan the entire FBZ. The IBZ presents the smallest part of the FBZ that makes it possible to reproduce the FBZ by mirroring and rotating. If elements e_1, e_2, e_3, and e_4 in Fig. 1 have the same deterministic mechanical property distribution and geometric characteristics with respect to the frame center (node q_1), which is the case in the deterministic analysis of the present study, it is known that the IBZ contour can be used. On the other hand, if these four elements are (or there is a possibility of being) different, e.g., there is significant variability related to the manufacturing of these elements, the literature indicates that the FBZ should be used instead of the IBZ contour [65].

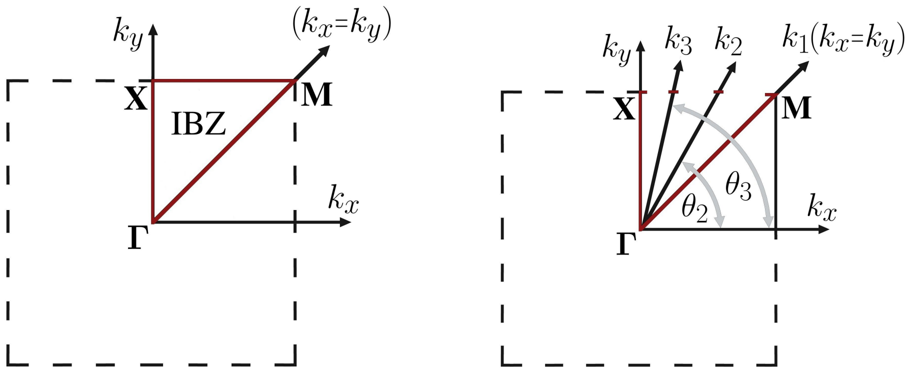

(a) Representation of the FBZ and IBZ (contour in red) in the reciprocal space.

(b) Representation of the samples made in the contour line $\mathbf{M}-\mathbf{X}$ in the IBZ.

Figure 4: Representation of the IBZ for the proposed two-dimensional frame cell (a), and the proposed observations along the contour line from $\mathbf{M}$ to $\mathbf{X}$ (b).

The direction of the k_x and k_y axes can be changed using the same samples presented in Fig. 4b to compute the FBZ contour, as presented in Appendix D and Appendix H.

Figure 5 was obtained by applying the proposed procedure to determine the attenuation using the IBZ of the deterministic two-dimensional cell (Fig. 2a). Note that $\min(|\operatorname{Im}(kL)|)$ in Fig. 3 is the same as the first result ($\theta = 45°$) for the contour $\mathbf{\Gamma}-\mathbf{M}$ in Fig. 5. It is possible to observe that there are four large complete and full attenuation bands where the attenuation per cell length is at least 20%: 2.45-4.28 kHz; 4.60-6.35 kHz; 11.45-14.40 kHz; 14.85-19.35 kHz, and four band of at least 60% of attenuation per cell length: 2.90-4.10 kHz; 4.88-6.03 kHz; 12.00-14.10 kHz; 15.10-18.40 kHz.

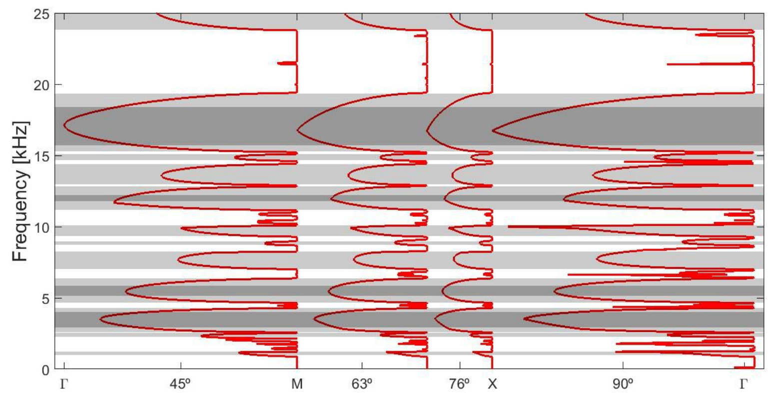

Figure 5: Minimum of the magnitude of the imaginary part of the wavenumber along the contour of the IBZ for the cell represented in Figure 2 from 0 to 25 kHz. Attenuation per cell length of at least 20% (light gray) and 60% (middle gray).

3.2. Simulating a two-dimensional metastructure

The dispersion relation computed from the unit cell can be used to interpret or predict attenuation even in more complex structures, requiring a larger computational cost. Such as the structure shown in Fig. 6. It is composed of 16 two-dimensional cells, with excitation in the left bottom corner. Figure 7 presents the accelerance frequency response function (FRF) at an upper node superposed at the attenuation patches from Fig. 5. It is possible to observe that there is strong attenuation within the predicted attenuation zones, corroborating the previous results of the periodic cell wavenumber analysis (Fig. 5).

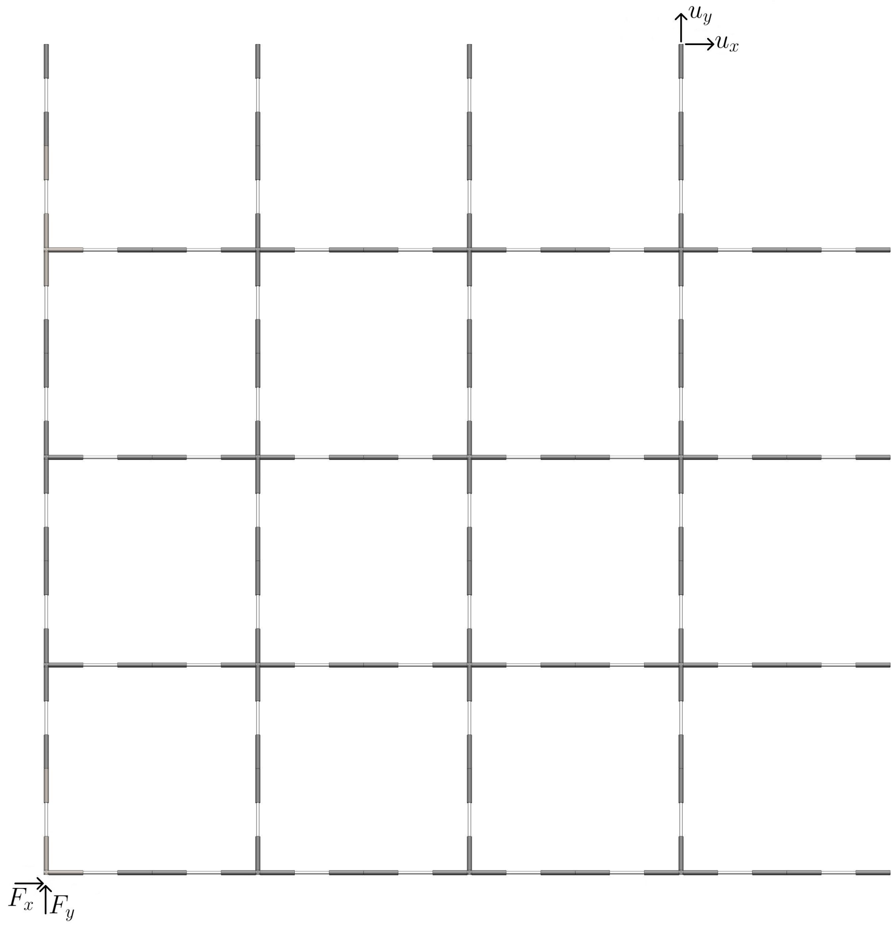

Figure 6: Proposed metastructure excited at the base (F_x and F_y) with response at the top (u_x u_y).

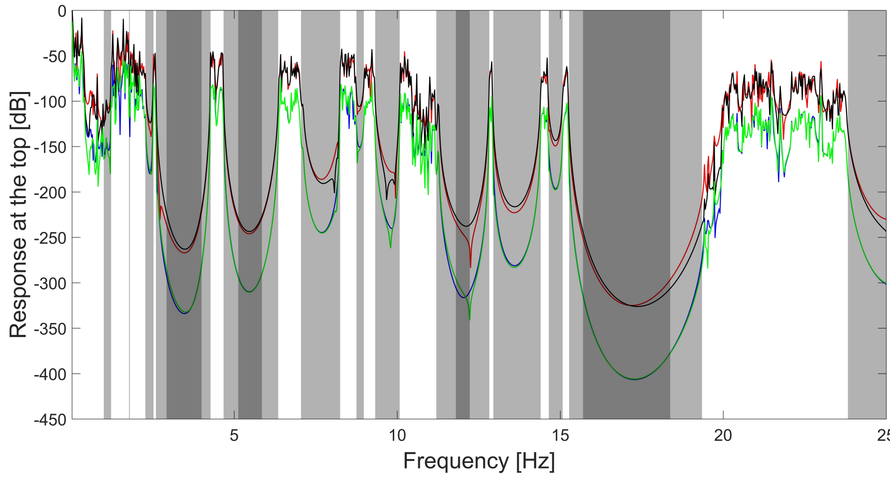

Figure 7: Obtained FRF for the proposed two-dimensional structure in Fig. 6. For horizontal excitation (F_x), the FRFs in red and blue are for vertical (u_y) and horizontal (u_x) responses respectively. For vertical excitation (F_y), the FRFs in black and green are for vertical (u_y) and horizontal (u_x) responses respectively. Attenuation per cell length of at least 20% (light gray) and 60% (middle gray).

Figure 8 compares the FRF of the proposed metastructure (Fig. 6) constituted by frame elements made of two materials (Fig. 1a) represented by the blue line, the homogeneous nylon frame represented by the red line, and the homogeneous aluminum frame represented by the green line. It is possible to notice one main attenuation band beginning at approximately 14 kHz and five narrower attenuation bands beginning at approximately 2.5 kHz, 4.5 kHz, 6 kHz, 12 kHz, and 13.5 kHz, respectively.

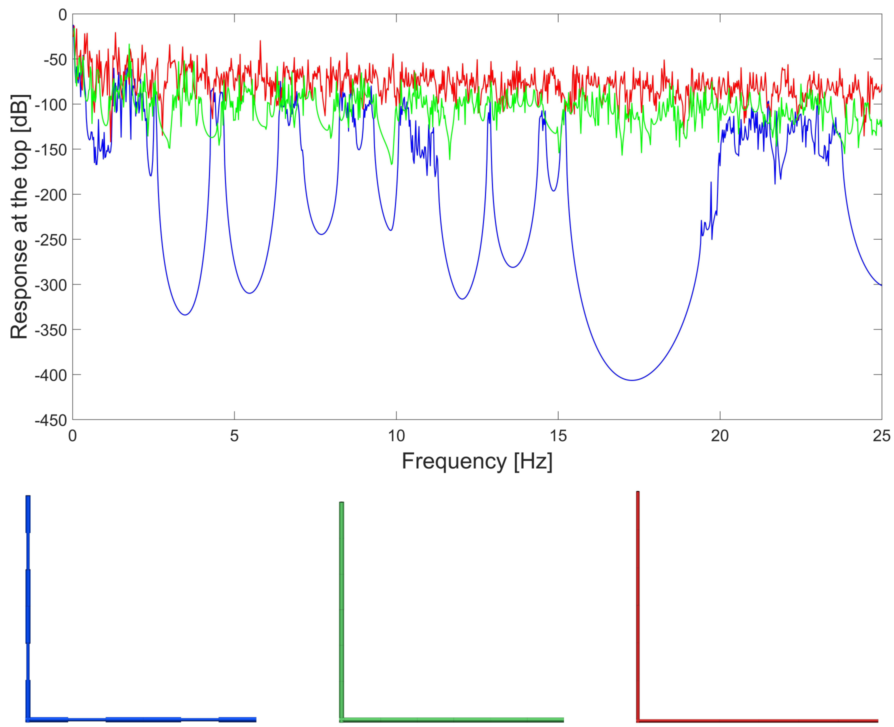

Figure 8: FRFs for vertical excitation and vertical response of the proposed metastructures (Fig. 6) with frame elements made of: nylon and aluminum (Fig. 3) (blue), homogeneous aluminum (green), and homogeneous nylon (red).

So far, the deterministic results can be summarized as follows: it is possible to verify the vibration response, especially attenuation bands, of a two-dimensional periodic frame structure by analyzing its unit cell only. In addition, if the unit cell has certain geometric and mechanical property symmetries, results for the IBZ are equivalent to results for the FBZ as expected. The computational cost of analyzing attenuation bands throughout the IBZ of the unit cell is substantially smaller than computing the FRFs of the metastructures. For stochastic analyses, where the simulations have to be performed several times, this can be of utmost importance. In the next section, some stochastic results are presented for metastructures considering attenuation bands and FRFs for periodic and non-periodic geometries. The different attenuation bands are compared among themselves and with these FRFs in order to verify how robust can the attenuation band be against the proposed variability.

4. Assuming randomness at mechanical properties

As the geometric and/or mechanical property variability of a certain sample can be asymmetric, the use of the IBZ instead of the FBZ cannot, in principle, be made. However, when the variability (not the individual sample, but among several samples) is analyzed as a whole, and the aim is to define attenuation bands that are robust against such variability, the stochastic FRFs of metastructures coincide with the results for the IBZ of a frame cell under variability. These results will be presented in the current section.

4.1. Statistical inference

The usual confidence interval [25] is not suitable for the desired type of inference, because the aim is to achieve the interval between the minimum and maximum attenuation, not to know the minimum possible attenuation. In addition, usual statistical tests [21] and an inference methodology with a more straightforward interpretation could be the best choice. Thus, in the present study, we infer the stochastic results using the ratio of chances, which is similar to using the Bayes' factor (BF) [22] in Bayesian statistics [25]. This inference consists of testing the null (H_0) against the hypothesis (H_1) in the following way:

$$H_0 : \beta \in \beta_0 \text{ vs } H_1 : \beta \in \beta_1, \tag{10}$$

where $\beta_0 \cup \beta_1 = B$, where B is the parameter space, $\beta_0 \cap \beta_1 = 0$. Considering $\pi(\beta_1)$ the probability of occurring H_1 and $\pi(\beta_0)$ the probability of occurring H_0, $BF_{1,0}$ is defined as

$$BF_{1,0} = \frac{\pi(\beta_1)}{\pi(\beta_0)}, \tag{11}$$

where the value of $BF_{1,0}$ establishes quantitatively how many times is the evidence H_1 stronger than H_0. The so-called Jeffreys' scale of evidence, which links quantitative intervals of Bayes' factor to qualitative evidence was used in current study. This scale is presented in Table 1.

Table 1: Jeffreys' scale of evidence.

FB value	Evidence against H_0
$1 \sim 3$	weak
$3 \sim 10$	moderate
$10 \sim 30$	substantial
$30 \sim 100$	strong
> 100	decisive

Table 1 can be used to create credibility intervals, hypothesis tests or in optimization. In practice, the $BF_{1,0}$ can be applied to the stochastic $min(\mid \mathrm{Im}(k) \mid)$ throughout the stochastic dispersion relation, using $H_0 : min(\mid \mathrm{Im}(k) \mid) > \delta_k$, to indicate how many times the attenuation band is more likely to occur than not to occur.

There are cases where the variability of the mechanical properties is considerably smaller within batches than between batches, such as, in concrete manufacturing [66] or for natural composite materials, such as bamboos, where the mechanical property variability can be almost homogeneous for a given section but can vary along with the plant height, and it can vary considerably from plant to plant [67]. For such type of variability, it is reasonable to assume the same mechanical property along a given frame section, but different for different sections of different batches.

4.2. Simulating the spatial fields

Typically, mechanical properties vary throughout the structure manufactured via additive manufacturing [68, 69, 70]. One possible approach for taking this into account consists in using a statistical tool to simulate a stochastic field along the structure length, related to the spatial covariance and the known (or estimated) spatial variability [71]. The EOLE [72] method can be used in such cases in a more efficient way. In this case, similarly to the discrete Karhunen–Loève expansion [40, 71], a correlation matrix, using a discretized space can be used to generate the correlation matrix $\mathbf{\Sigma}$, built via assuming a known correlation function. Then, eigenvalues ($\hat{\boldsymbol{\lambda}}$) and eigenvector ($\hat{\boldsymbol{\psi}}$) are computed assuming a certain correlation length $L_c = L_x/2 = L_y/2$ (the frame length, see Fig. 1) [71].

$$\hat{\mathbf{\Sigma}}\hat{\boldsymbol{\psi}}L_c = \hat{\boldsymbol{\lambda}}\hat{\boldsymbol{\psi}}. \tag{12}$$

In addition, a set of n samples from a given spatial random field discretized into p elements is defined as $\mathbf{X}_o^T$. Hence, the term $\mathbf{X}_0^T$ is a $n' \times p'$ matrix, where n' is the sample size and p' is the discretization number. Finally, the process mean $\mu_y(x)$ is the mean of the simulated spatial random variable along the entire frame length. When dealing with experimental data, the distribution of $\mathbf{X}_0^T$ can be estimated in a highly precise way using a Bayesian estimator [27] as briefly presented in [10]. Finally, the mean-centered correlated random variable (Z_i) can be defined as [73]

$$Z_i = \frac{1}{\sqrt{\lambda_i}}\boldsymbol{X}_0^T\psi_i\hat{\mathbf{\Sigma}}, \tag{13}$$

where, analogously to the KL expansion truncated in k terms, the EOLE can be determined by Eq. (14) [40]. In the current study, it was defined $k = 8$, and the spatial mean ($\mu_y(x)$) is finally added to the mean-centered correlated random variable.

$$Y(x) = \mu_y(x) + \sum_{i=1}^{k} Z_i, \tag{14}$$

where $\mu_y(x)$ is the field mean value and the correlation function is given, in a piece-wise form, by the exponential function, between two discrete spatial positions ($x(i)$ and $x(j)$) used to create $\hat{\mathbf{\Sigma}}$

$$exp\left(-\frac{\mid (x(i) - x(j) \mid}{L_c/2}\right), \tag{15}$$

where $i = 1, 2, ..., n' - 1$. In the present study, the value $n' = 120$ was considered. The greater the n', the greater the discretization of the spatial field.

The exponentially decaying correlation function was chosen because it is commonly used to represent spatial correlation of random fields in engineering [71] and, particularly, to characterize the spatial correlation of mechanical properties [5, 74].

4.3. Comparing stochastic results

In the current study, it was observed that, usually, if a deterministic one-dimensional frame element presents a band gap for all waves in a certain frequency band, the two-dimensional frame cell will present a full and complete band gap near that frequency band. Three configurations are proposed as PC frame elements (Fig. 1b) to build the two-dimensional unit cell (Fig. 1a). All the frame elements have a circular cross-section. We used two different beam theories and different types of variability in order to verify if the same behavior was consistently observed. The first two frame elements, shown in Fig. 2b (with segments f_1 and f_2) and in Fig. K.1a (with segments f_3 and f_4), were modeled using the EB beam theory, while the third (Fig. 9) was modeled using the Timoshenko beam theory (with only one segment f_5). Segment f_5 is made of nylon and was defined using a Fourier series to represent the spatial radius ($r(x)$) and performing an optimization aiming at a wider and lower frequency band gap. The optimization procedure is described in [75, 76].

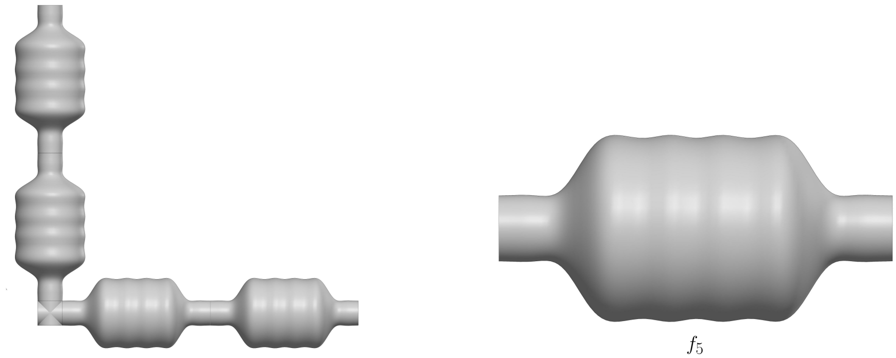

(a) (b)

Figure 9: Another proposed unit cell made of four frame elements modeled via: (a) elementary rod and T beam theories. The defined frame elements of nylon have (b) a spatially varying cross-sectional area.

The mechanical and geometric characteristics of segments f_1, f_2, f_3, and f_4 are summarized in Table 2. The terms X_1, X_2, X_3, and X_4 are Gamma distributions (Gamma(α_x, β_x)) with shape parameter α_x and scale parameter β_x. The Gamma distribution is used here because it is versatile and suitable for positive value distributions [71]. In the present study, we defined $X_1 \sim$ Gamma$(1, 5)$, $X_2 \sim$ Gamma$(2, 10)$, $X_3 \sim$ Gamma$(10, 0.5)$, and $X_4 \sim$ Gamma$(10, 1)$. With such different values, the random variables of ρ and E are considerably different between the two frame elements. The first frame is associated with a larger variability (related to X_1 and X_2) than the second and third ones (related to X_3 and X_4). The term $r(x)$ represents a spatially varying radius given by Fourier series that are optimized for lower and wider full attenuation zones (see [75, 76]). Note that no geometric variability is considered.

	Configuration 1		Configuration 2		Configuration 3
	f_1	f_2	f_3	f_4	f_5
ρ [kg/m3]	1200	2700	1200(1+X_3)	1200(1+X_3)	1200(1+X_4)
E [GPa]	2(1+X_1)	70(1+X_2)	3(1+X_4)	3(1+X_4)	2(1+X_3)
G [GPa]	-	-	-	-	$\frac{\mathrm{E}(1+X_3)}{(2(1+nu))}$
ν [1]	-	-	-	-	0.35
L [mm]	60	60	70	150	180
r [mm]	2.5	4	3	6	r(x)

Table 2: Mechanical and geometric characteristics of the first two proposed frame elements with varying mechanical properties.

The MC method [77, 78] is combined with the EOLE expansion procedure and the dispersion relation and metastructure models are used to simulate the stochastic results of configuration 3. The MC mean and variance convergences were also investigated but not shown here. Details of the inference using BF on the stochastic dispersion relation for the first two-dimensional frame cell shown in Fig. 2 for configuration 1 can be found in Appendix I. Results are obtained using the MC method with 4,000 field samples (1,000 steps with 4 different frames each as presented in Section 4.2).

Figure 15a presents the summary of the inference for configuration 1 using BF100 for the defined values of θ along the IBZ contour in the frequency range from 0 to 25 kHz. BF100 represents bands where the probability of an attenuation band of at least 20% (light gray) and 60% (middle gray) per cell length to occur is at least 100 times higher than not to occur. It is possible to observe that there are three robust attenuation bands of at least 60% per cell length from (3.13-4.18 kHz; 5.33-6.55 kHz; 17.00-19.60 kHz) against the material property variability. Observing the inference on the stochastic dispersion relation, it is possible to investigate the attenuation bands that are robust against the proposed variability in a more efficient way than considering the attenuation band width [10].

The equivalent result for the FBZ was obtained simulating 125 MC samples for the same four elements e_1, e_2, e_3, and e_4, which should yield the same result as 1,000 samples of the IBZ is presented in Fig. 15b. Eight MC samples on the IBZ are equivalent to one sample on the FBZ considering the spatial mechanical properties of elements e_1, e_2, e_3, and e_4 are defined randomly and independently of each other. Each sample of the MC method response when using the FBZ contour was calculated using the same elements e_1, e_2, e_3, and e_4 on the two-dimensional frame cell, by rotating 180° on the y direction, calculating the stochastic response, rotating 90° on the z direction, and calculating the stochastic response. After this procedure is performed four times, the result for the full sweep of the IBZ was obtained. There are also three attenuation bands of at least 60% per cell (3.05-4.30 kHz; 5.05-6.25 kHz; 10.15-10.22 kHz; 17.00-19.63 kHz).

The stochastic result consists of inferring on the result of 1,000 two-dimensional frame cells. The first two two-dimensional frame cells are presented in Fig. 10 for configuration 1. It is possible to observe that none of these two-dimensional frame cells, and possibly none of the other 1,000 samples, is symmetric on the x and y directions (4-fold deterministic symmetry), which is a necessary condition for the use of the IBZ contour shown in Fig. 4b. However, when dealing with statistical analyses, the distribution should be analyzed, not the individual samples. Thus, it is possible to observe that there is a symmetry of the distributions of E throughout the cell by looking at Fig. 11, which represents the distributions as histograms for each segment. This can explain the similarity between the inference on the stochastic FBZ and corresponding IBZ.

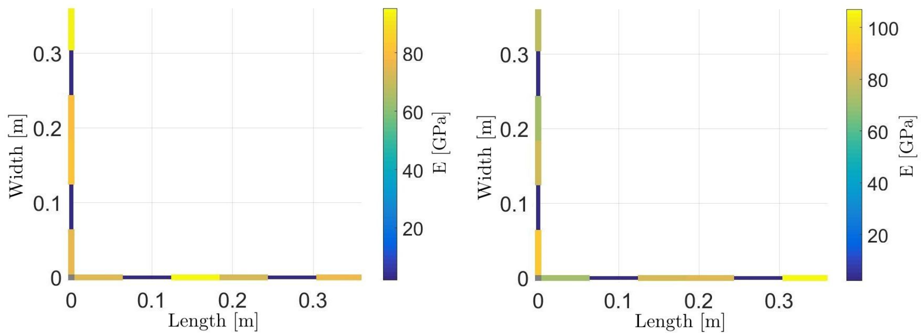

Figure 10: First two samples of the first frame cell (Fig. 2a) with E following the distributions of f_1 and f_2 stated in Table 2.

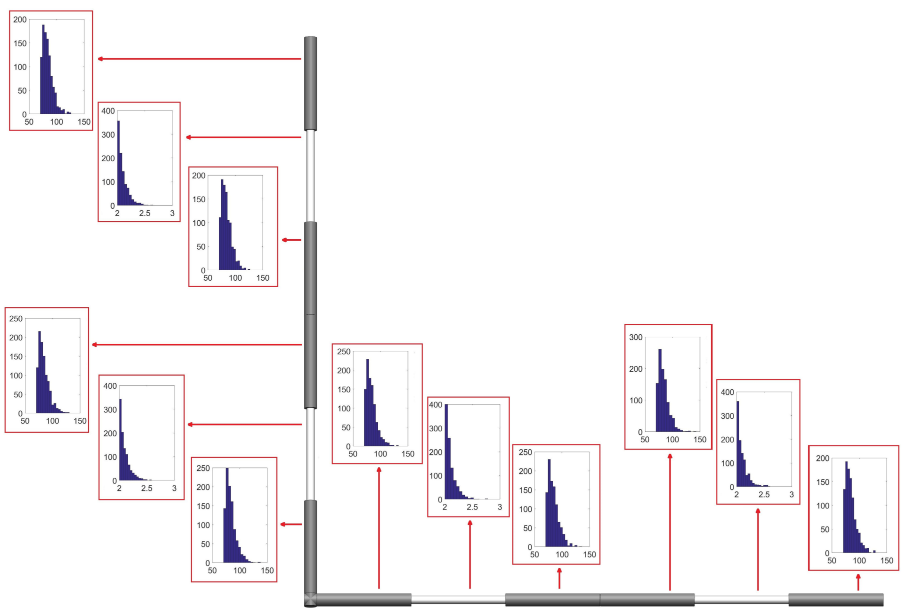

Figure 11: Histograms representing the distributions of the sampled values used to simulate the stochastic response of E on the first sampled two-dimensional frame cell.

The same procedure was applied to Fig. 9b For configuration 3 with spatial variability of E, ρ, and G modeled via EOLE method, with the spatially correlated samples defined according to the distributions on segment f_5 of Table 2.

The inference using BF100 on the stochastic results for the IBZ and equivalent FBZ are graphically represented respectively in Fig. 17a and Fig. 17b. Again, when considering individual observations there is no symmetry in the spatial variability of E, ρ or G. Fig. 12 presents the first two samples of the three spatial varying mechanical properties. But when looking at their spatial distribution of such variability in Fig. 13, it is possible to verify the symmetry-related to all these spatial variability. This result agrees with previously observed results for uncertainty in mass, damping, and stiffness matrices in the scattering properties of the mechanical joints [44]. It helps to understand the similarity between stochastic IBZ and FBZ dispersion under symmetry of distributions, even though individual samples are not symmetric. It is possible to notice an overall agreement between the robust attenuation bands computed along the IBZ and FBZ, specially in the main robust attenuation bands of at least 20% per cell: 6.50-7.23 kHz, and of at least 60%: 1.92-3.73 kHz; 15.20-15.60 kHz; 4.00-4.30 kHz

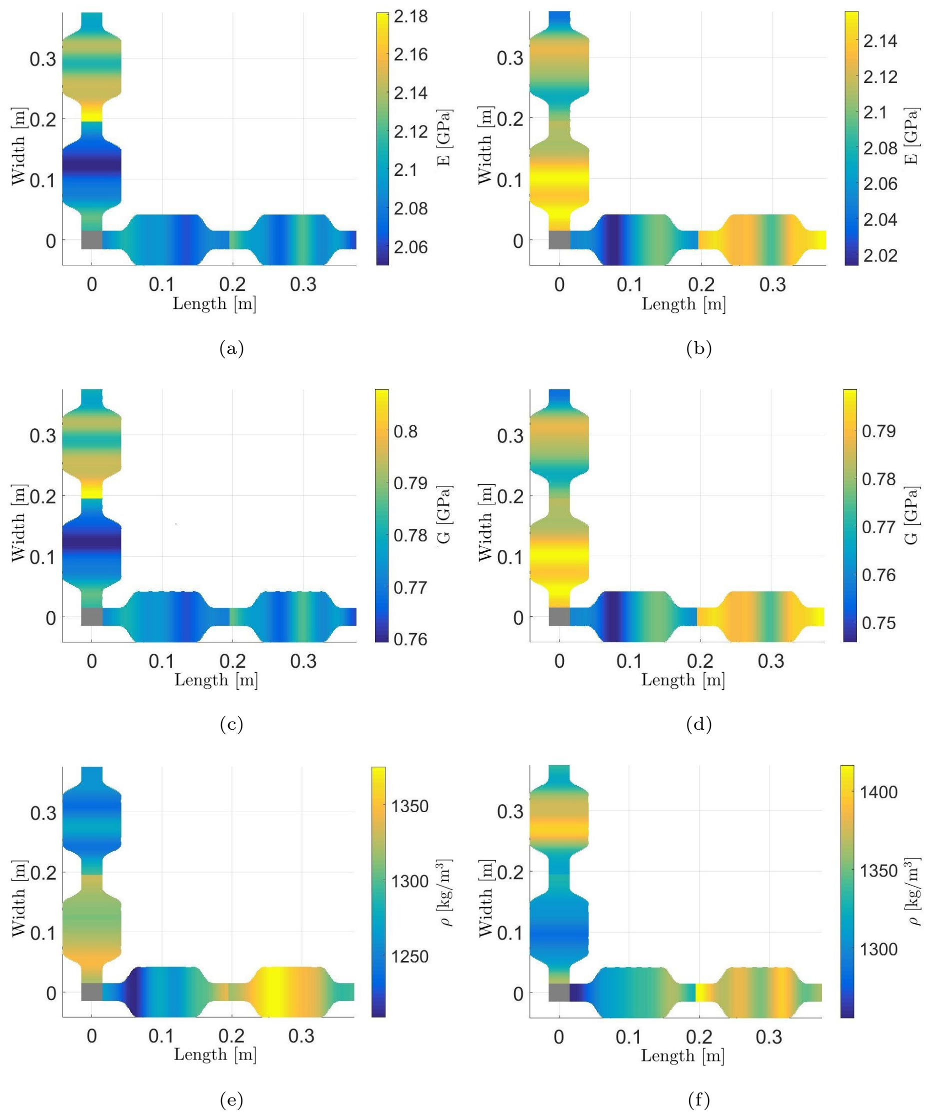

Figure 12: First two samples of the first frame cell (Fig. 9b) with $E(x)$ (a-b), $G(x)$ (c-d), and $\rho(x)$ (e-f) following the distribution of f_5 stated in Table 2.

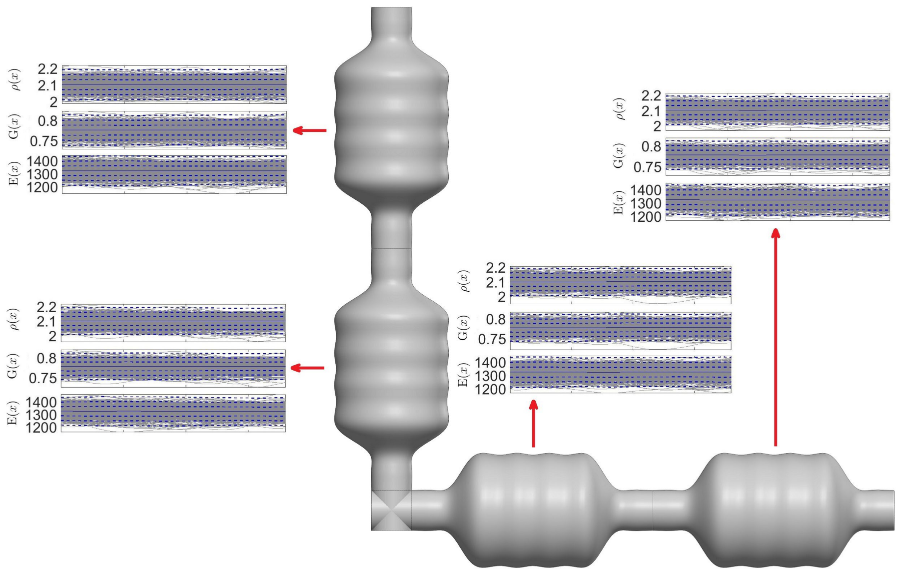

Figure 13: The proposed two-dimensional frame cell with spatially varying mechanical properties and their associated simulated fields represent the symmetric spatial variability of the mechanical properties.

For configuration 2, the same results shown for configurations 1 and 3 are shown in Appendix J, where the same stochastic results are shown for a different frame element with variability in E and ρ, as presented in Table 2, also modeled using elementary rod and EB beam theories. However, even though the stochastic results along the FBZ and IBZ contour agree, indicating that the IBZ can be used under symmetry of variability, it is worth investigating if the wavenumber analysis can represent metastructures under periodicity of variability.

4.4. Analyzing the wave attenuation attenuation using a supercell

Figure 14 is a scheme of a supercell made of 9 fundamental cells via assembling 36 frame elements in 33 nodes. Now, the first proposed two-dimensional frame cell element (Fig. 2a) is used, the random mechanical property of each frame is a sample of the mechanical property distribution shown in Table 2. The external nodes (red) were maintained to obtain the dispersion diagram, the other 21 nodes were condensed in a similar way as presented in Appendix C. Further details of the Bloch-Floquet periodic conditions modeling of the proposed supercell are presented in Appendix K.

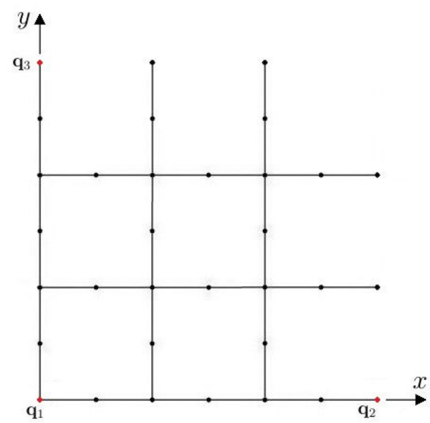

Figure 14: Schematic representation of super-cell used to calculate the stochastic dispersion diagram. Only the red nodes (at the boundaries) were considered and the internal nodes were condensed to reduce the order of the polynomial.

For configuration 1, Figure 15c presents graphically the same procedure for measuring the attenuation related to the proposed two-dimensional supercell. One can notice good agreement between Fig. 15c, Fig. 15a, and Fig. 15b. In Fig. 15c, there are other attenuation bands and attenuation bands of at least 60% wider than the ones presented in Fig. 15a, which occurs because the supercell is more complex and larger than the unit cell [1]. However, the attenuation bands predicted using the unit cell occur on the supercell. The same can be observed and concluded when comparing the inference on the stochastic attenuation of the supercell response made of the third proposed frame with spatially varying mechanical properties for configuration 3 (Fig. 9b). This result is graphically represented in Fig. 17c that can be compared to the results obtained using the unit cell in Fig. 17a and Fig. 17b.

4.5. Comparing the stochastic forced responses

Figures 15 and 17 present comparisons of the attenuation bands throughout the stochastic IBZ and FBZ contours inferred using the frame cell (Fig. 1a) and the IBZ contour inferred using the supercell (Fig. 14) for the frame elements in Fig. 2b and Fig. 9b, respectively. It is possible to verify that the three results agree, even though frame samples with different mechanical properties were simulated and, thus, a certain level of difference between different simulations is expected, even after achieving convergence. The 500 forced responses of the metastructure with 64 frame elements (Fig. 6) are shown in Fig. 16. It is possible to verify the agreement between attenuation bands computed using the unit cells and stochastic FRFs computed using the finite metastructure. Results for the third proposed frame element are presented in Appendix J.

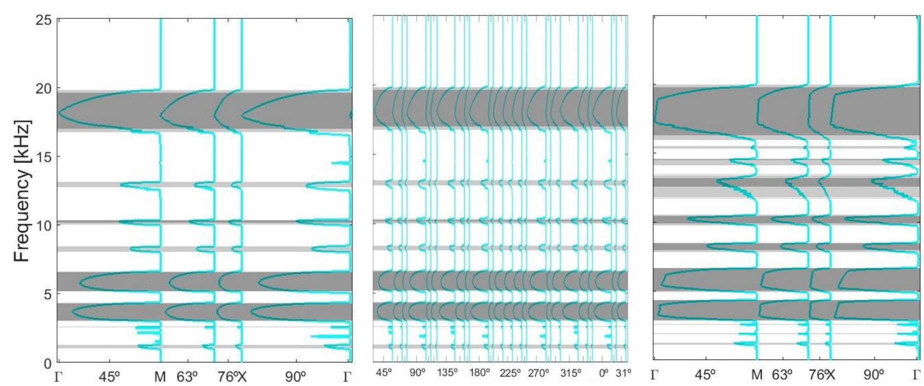

(a) (b) (c)

Figure 15: Minimum value of the magnitude of the imaginary part throughout the IBZ (a) and FBZ contours (b) computed using the unit cell (Fig. 1a) and the IBZ contour (c) computed using the supercell (Fig. 14), using the frame element in Fig. 2b. The patches represent the IBZ attenuation per cell length of at least 20% (light gray) and 60% per cell (dark gray).

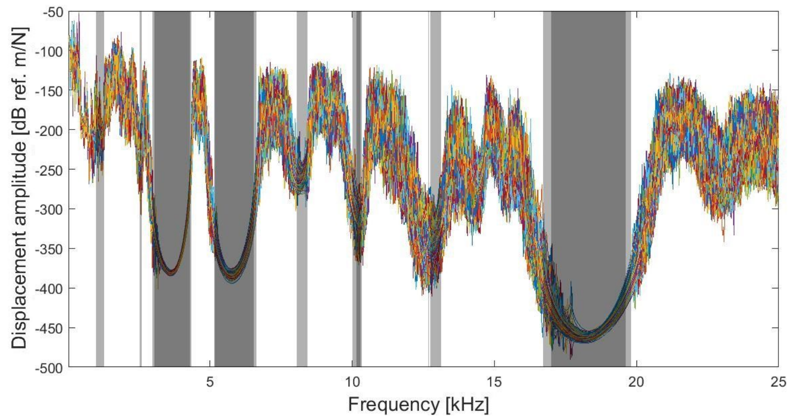

Figure 16: Stochastic FRFs computed for 500 samples of the proposed metastructure (Fig. 6, vertical excitation and vertical response) made of 16 two-dimensional frame cells (Fig. 2b) with the inference made on the stochastic IBZ of a single unit cell. The patches represent an attenuation per cell length of at least 20% (light gray) and 60% per cell (dark gray).

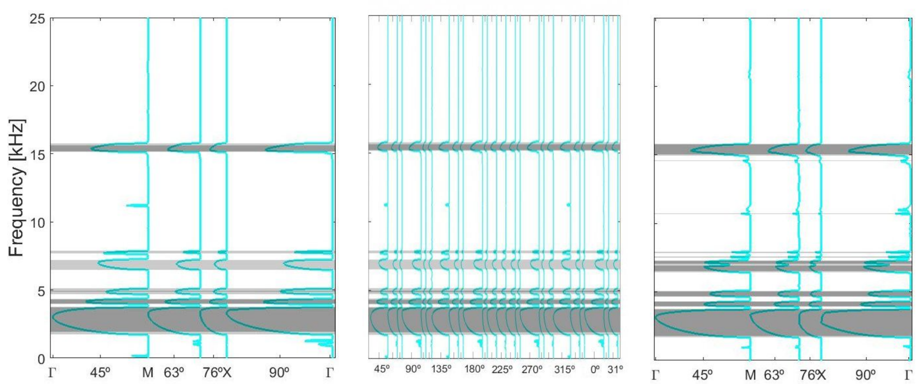

(a) (b) (c)

Figure 17: Minimum value of the magnitude of the imaginary part throughout the IBZ (a) and FBZ contours (b) computed using the unit cell (Figure 1a) and the IBZ contour (c) computed using the supercell (Fig. 14), using the frame cell in Fig. 9b. The patches represent the IBZ attenuation per cell length of at least 20% (light gray) and 60% per cell (dark gray).

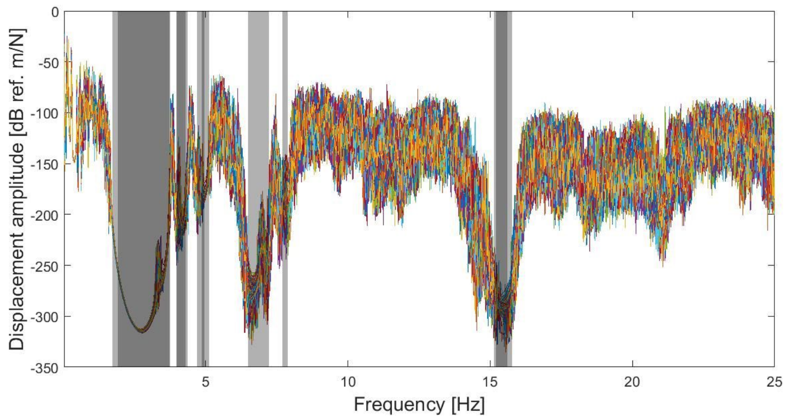

Figure 18: Stochastic FRFs computed for 500 samples of the proposed metastructure (Fig. 6, vertical excitation and vertical response) made of 16 two-dimensional frame cells (Fig.9b) with the stochastic IBZ of a single unit cell. The patches represent the IBZ attenuation per cell length of at least 20% (light gray) and 60% per cell (dark gray).

The results presented in the current section show that, under 4-fold symmetry of variability, the inference on the stochastic IBZ contour computed using the frame cell can be used to predict robust attenuation bands in finite metastructures. These stochastic results agree with the results for the FBZ contour computed using the unit cell, the IBZ computed using the supercell, and the FRFs of the finite metastructure. However, the computational cost is much lower when using the IBZ contour than with the other methods. This can be illustrated by the number of frame element samples used in each simulation. The IBZ contour using the frame cell used 4,000 samples, while the stochastic IBZ for the supercell used 36,000 samples, and the stochastic FRFs used 32,000 samples.

5. Final remarks

Beyond the deterministic case, where the IBZ corresponds to the FBZ for periodic structures with geometric and mechanical property 4-fold rotational symmetry of their unit cell, the presented results indicate that the stochastic analysis on the IBZ of the unit cells and supercells, and on the FBZ of the unit cells are equivalent when there is 4-fold rotational symmetry of variability of the frame cell. This methodology was applied to different two-dimensional rectangular frame cells, and it was shown that, by analyzing the two-dimensional unit cell alone, it is possible to accurately predict the vibration attenuation bands in metastructures under 4-fold rotational symmetry of variability. We have used two types of variability: homogeneous sections and homoscedastic fields (constant variance), but this property might also apply to other kinds of periodic structures (e.g., plates) and other types of rotational symmetry of variability. However, this is outside the scope of the current work.

A two-dimensional stochastic modeling procedure for wave propagation analysis of plane frame lattices is proposed. The methodology consists of a combination of SEM with the solution of the polynomial equation yielded by applying the Bloch-Floquet theorem to the frame element dynamic stiffness matrix. It is compatible with stochastic modeling because it is computationally efficient and presents straightforward indications of full and complete attenuation bands. This methodology is applied to the dispersion diagrams of the unit-cell and the supercell and to the forced response of three different frame metastructures.

In addition, in the present work, a method to determine wave band gaps of a two-dimensional unit frame cell modeled using SEM is presented. It consists of computing the minimum of the magnitude of the imaginary part of the wavenumbers along the IBZ contour. This procedure can be used for structures modeled via SEM in a computationally efficient way, which is of utmost importance when dealing with statistical analyses. A highly precise Bayesian estimator is used to infer the material property variability and the stochastic responses.

Acknowledgments

The authors gratefully acknowledge the financial support of the São Paulo Research Foundation (FAPESP) through processes number 2019/00315-8, 2018/18774-

6 and 2018/15894-0, and the Brazilian National Council of Research CNPq (Grant Agreement IDs: 420304/2018-5 and 305293/2021-4).

References

[1] D. Beli, A. T. Fabro, M. Ruzzene, J. R. F. Arruda, Wave attenuation and trapping in 3D printed cantilever-in-mass metamaterials with spatially correlated variability, Scientific reports 9 (1) (2019) 5617.

[2] J. P. Wolf, G. R. Darbre, Dynamic-stiffness matrix of soil by the boundary-element method: Conceptual aspects, Earthquake engineering & structural dynamics 12 (3) (1984) 385–400.

[3] A. T. Fabro, H. Meng, D. Chronopoulos, Uncertainties in the attenuation performance of a multi-frequency metastructure from additive manufacturing, Mechanical Systems and Signal Processing 138 (2020) 106557.

[4] Z. Zhang, T. Li, Z. Wang, Y. Tang, Band gap characteristics of flexural wave of two-dimensional periodic frame structure composed of locally resonant composite beam, Mechanical Systems and Signal Processing 131 (2019) 364–380.

[5] A. T. Fabro, D. Beli, J. R. F. Arruda, N. Ferguson, B. Mace, Uncertainty analysis of band gaps for beams with periodically distributed resonators produced by additive manufacturing, in: ISMA 2016 Conference on Noise and Vibration Engineering. Leuven, Belgium, 2016.

[6] U. Lee, J. Kim, H. Oh, Spectral analysis for the transverse vibration of an axially moving timoshenko beam, Journal of Sound and Vibration 271 (3-5) (2004) 685–703.

[7] O. Aklouche, A. Pelat, S. Maugeais, F. Gautier, Scattering of flexural waves by a pit of quadratic profile inserted in an infinite thin plate, Journal of Sound and Vibration 375 (2016) 38–52.

[8] C. Zhao, M. G. Prasad, Acoustic black holes in structural design for vibration and noise control, in: Acoustics, Vol. 1, Multidisciplinary Digital Publishing Institute, 2019, pp. 220–251.

[9] G. Carta, G. F. Giaccu, M. Brun, A phononic band gap model for long bridges. the ‘brabau’bridge case, Engineering Structures 140 (2017) 66–76.

[10] L. H. M. S. Ribeiro, V. F. Dal Poggetto, D. Beli, A. Fabro, J. R. F. Arruda, A two-dimensional lattice with band gaps robust to me-chanical variability, in: ISMA 2020 Conference on Noise and Vibration Engineering. Leuven, Belgium, Vol. 16, 2020.

[11] G. Mitrou, N. Ferguson, J. Renno, Wave transmission through two-dimensional structures by the hybrid fe/wfe approach, Journal of Sound and Vibration 389 (2017) 484–501.

[12] M. Collet, M. Ouisse, M. Ruzzene, M. Ichchou, Floquet–bloch decomposition for the computation of dispersion of two-dimensional periodic, damped mechanical systems, International Journal of Solids and Structures 48 (20) (2011) 2837–2848.

[13] X. He, W. He, J. Shi, C. Sun, Boundary vibration control of variable length crane systems in two-dimensional space with output constraints, IEEE/ASME Transactions on Mechatronics 22 (5) (2017) 1952–1962.

[14] B. R. Mace, E. Manconi, Modelling wave propagation in two-dimensional structures using finite element analysis, Journal of Sound and Vibration 318 (4-5) (2008) 884–902.

[15] W. Elmadih, D. Chronopoulos, W. Syam, I. Maskery, H. Meng, R. Leach, Three-dimensional resonating metamaterials for low-frequency vibration attenuation, Scientific reports 9 (1) (2019) 1–8.

[16] Z. Jia, Y. Chen, H. Yang, L. Wang, Designing phononic crystals with wide and robust band gaps, Physical Review Applied 9 (4) (2018) 044021.

[17] S. Ahsani, L. Van Belle, C. Claeys, W. Desmet, E. Desmet, The effect of geometrical variability on the sound absorption performance of meta-poro-elastic systems with small mass inclusions, in: INTER-NOISE and

NOISE-CON Congress and Conference Proceedings, Vol. 261, Institute of Noise Control Engineering, 2020, pp. 5474–5485.

[18] M. Machado, S. Adhikari, J. Dos Santos, J. Arruda, Estimation of beam material random field properties via sensitivity-based model updating using experimental frequency response functions, Mechanical Systems and Signal Processing 102 (2018) 180–197.

[19] M. R. Souza, D. Beli, N. S. Ferguson, J. R. d. F. Arruda, A. T. Fabro, A bayesian approach for wavenumber identification of metamaterial beams possessing variability, Mechanical Systems and Signal Processing 135 (1) (2020) 1–15.

[20] L. H. M. S. Ribeiro, V. F. Dal Poggetto, D. Beli, A. T. Fabro, J. R. F. Arruda, Bayesian statistics of uncertainty quantification attenuation bands of three-dimensional phononic lattices, in: Proceedings of the Ibero-Latin-American Congress on Computational Methods in Engineering, Vol. 41, Ibero-Latin-American Congress on Computational Methods in Engineering, 2020.

[21] A. M. Mood, F. A. Graybill, D. C. Boes, Introduction to the Theory of Statistics, 1973.

[22] C. Robert, The Bayesian choice: from decision-theoretic foundations to computational implementation, Springer Science & Business Media, 2007.

[23] R. d. O. Teloli, S. da Silva, T. G. Ritto, G. Chevallier, Bayesian model identification of higher-order frequency response functions for structures assembled by bolted joints, Mechanical Systems and Signal Processing 151 (2021) 107333.

[24] C. B. Goates, S. D. Sommerfeldt, J. D. Blotter, Frequency trends of acoustic radiation modes for cylindrical structures, in: Proceedings of Meetings on Acoustics 176ASA, Vol. 35, Acoustical Society of America, 2018, p. 065003.

[25] H. Jeffreys, Theory of Probability, 3rd Edition, Oxford University Press, 1961.

[26] P. Congdon, Applied bayesian modelling, Vol. 595, John Wiley & Sons, 2014.

[27] L. H. M. S. Ribeiro, V. F. Dal Poggetto, D. Beli, A. T. Fabro, J. R. F. Arruda, Investigating the influence of mechanical property variability on dispersion diagrams using bayesian inference, in: 5th International Symposium on Uncertainty Quantification and Stochastic Modeling (Uncertainties 2020), 2020.

[28] L. D'Alessandro, E. Belloni, R. Ardito, A. Corigliano, F. Braghin, Modeling and experimental verification of an ultra-wide bandgap in 3D phononic crystal, Applied Physics Letters 109 (22) (2016) 221907.

[29] L. D'Alessandro, B. Bahr, L. Daniel, D. Weinstein, R. Ardito, Shape optimization of solid–air porous phononic crystal slabs with widest full 3D bandgap for in-plane acoustic waves, Journal of Computational Physics 344 (2017) 465–484.

[30] N. Gao, Y.-l. Huang, R.-h. Bao, W.-q. Chen, Robustly tuning bandgaps in two-dimensional soft phononic crystals with criss-crossed elliptical holes, Acta Mechanica Solida Sinica 31 (5) (2018) 573–588.

[31] H. Jiang, Y. Wang, Phononic glass: A robust acoustic-absorption material, The Journal of the Acoustical Society of America 132 (2) (2012) 694–699.

[32] L. D'Alessandro, R. Ardito, F. Braghin, A. Corigliano, Low frequency 3D ultra-wide vibration attenuation via elastic metamaterial, Scientific reports 9 (1) (2019) 1–8.

[33] Z. Jia, Y. Chen, H. Yang, L. Wang, Designing phononic crystals with wide and robust band gaps, Physical Review Applied 9 (4) (2018) 044021.

[34] B. Xia, G. Wang, S. Zheng, Robust edge states of planar phononic crystals beyond high-symmetry points of brillouin zones, Journal of the Mechanics and Physics of Solids 124 (2019) 471–488.

[35] B.-Z. Xia, T.-T. Liu, G.-L. Huang, H.-Q. Dai, J.-R. Jiao, X.-G. Zang, D.-J. Yu, S.-J. Zheng, J. Liu, Topological phononic insulator with robust pseudospin-dependent transport, Physical Review B 96 (9) (2017) 094106.

[36] Y. Achaoui, V. Laude, S. Benchabane, A. Khelif, Local resonances in phononic crystals and in random arrangements of pillars on a surface, Journal of Applied Physics 114 (10) (2013) 104503.

[37] Z. Liu, X. Zhang, Y. Mao, Y. Zhu, Z. Yang, C. T. Chan, P. Sheng, Locally resonant sonic materials, Science 289 (5485) (2000) 1734–1736.

[38] B. Figeys, B. Nauwelaers, H. Tilmans, X. Rottenberg, Micromechanical ring resonators with a 2d phononic crystal support for mechanical robustness and providing mask misalignment tolerance, in: 2015 28th IEEE International Conference on Micro Electro Mechanical Systems (MEMS), IEEE, 2015, pp. 1016–1019.

[39] D. Schneider, F. Liaqat, E. H. El Boudouti, Y. El Hassouani, B. Djafari-Rouhani, W. Tremel, H.-J. Butt, G. Fytas, Engineering the hypersonic phononic band gap of hybrid bragg stacks, Nano letters 12 (6) (2012) 3101–3108.

[40] X. Zhang, J. He, A. Takezawa, Z. Kang, Robust topology optimization of phononic crystals with random field uncertainty, International Journal for Numerical Methods in Engineering 115 (9) (2018) 1154–1173.

[41] M. M. A. da Costa, D. A. Castello, C. Magluta, N. Roitman, On the optimal design and robustness of spatially distributed tuned mass dampers, Mechanical Systems and Signal Processing 150 (2021) 107289.

[42] A. T. Fabro, H. Meng, D. Chronopoulos, Correlated disorder in rainbow metamaterials for vibration attenuation, Proceedings of the Institution of

Mechanical Engineers, Part C: Journal of Mechanical Engineering Science 235 (14) (2021) 2610–2621.

[43] T. Chatterjee, S. Chakraborty, S. Goswami, S. Adhikari, M. I. Friswell, Robust topological designs for extreme metamaterial micro-structures, Scientific Reports 11 (1) (2021) 1–14.

[44] A. T. Fabro, J.-M. Mencik, On the non-parametric modelling of uncertain elastic joints in periodic structures, in: ISMA 2018 Conference on Noise and Vibration Engineering. Leuven, Belgium, 2018.

[45] R. R. Craig, A. J. Kurdila, Fundamentals of structural dynamics, John Wiley & Sons, 2006.

[46] R. D. Cook, et al., Concepts and applications of finite element analysis, John Wiley & Sons, 2007.

[47] K.-J. Bathe, Finite element procedures, Klaus-Jurgen Bathe, 2006.

[48] C. Zhou, X. Sun, J. Lainé, M. Ichchou, A. Zine, S. Hans, C. Boutin, Wave propagation feature in two-dimensional periodic beam lattices with local resonance by numerical method and analytical homogenization approach, International Journal of Applied Mechanics 10 (04) (2018) 1850042.

[49] M. I. Hussein, M. J. Leamy, M. Ruzzene, Dynamics of phononic materials and structures: Historical origins, recent progress, and future outlook, Applied Mechanics Reviews 66 (4) (2014).

[50] R. Langley, N. Bardell, H. Ruivo, The response of two-dimensional periodic structures to harmonic point loading: a theoretical and experimental study of a beam grillage, Journal of Sound and Vibration 207 (4) (1997) 521–535.

[51] E. Manconi, Modelling wave propagation in two-dimensional structures using a wave/finite element technique, Ph.D. thesis, Universita'di Parma. Dipartimento di Ingegneria Industriale (2008).

[52] D. S. Mackey, N. Mackey, C. Mehl, V. Mehrmann, Structured polynomial eigenvalue problems: Good vibrations from good linearizations, SIAM Journal on Matrix Analysis and Applications 28 (4) (2006) 1029–1051.

[53] K. M. Ahmida, J. R. F. Arruda, Spectral element-based prediction of active power flow in timoshenko beams, International Journal of Solids and Structures 38 (10-13) (2001) 1669–1679.

[54] G. Floquet, Sur les équations différentielles linéaires à coefficients périodiques, in: Annales scientifiques de l'École normale supérieure, Vol. 12, 1883, pp. 47–88.

[55] F. Bloch, Über die quantenmechanik der elektronen in kristallgittern, Zeitschrift für physik 52 (7-8) (1929) 555–600.

[56] M. Collet, M. Ouisse, M. Ruzzene, M. Ichchou, Floquet–bloch decomposition for the computation of dispersion of two-dimensional periodic, damped mechanical systems, International Journal of Solids and Structures 48 (20) (2011) 2837–2848.

[57] D. Magliacano, M. Ouisse, A. Khelif, S. De Rosa, F. Franco, N. Atalla, M. Collet, Computation of dispersion diagrams for periodic porous materials modeled as equivalent fluids, Mechanical Systems and Signal Processing 142 (2020) 106749.

[58] V. Romero-García, J. V. Sánchez-Pérez, S. Castiñeira-Ibáñez, L. M. Garcia-Raffi, Evidences of evanescent bloch waves in phononic crystals, Applied Physics Letters 96 (12) (2010) 124102.

[59] V. Romero-García, J. V. Sánchez-Pérez, L. M. Garcia-Raffi, Propagating and evanescent properties of double-point defects in sonic crystals, New Journal of Physics 12 (8) (2010) 083024.

[60] J. F. Doyle, Wave Propagation in Structures: A FFT-Based Spectral Analysis Methodology, Vol. 2, Springer, 1989.

[61] Y. Chen, X. Huang, G. Sun, X. Yan, G. Li, Maximizing spatial decay of evanescent waves in phononic crystals by topology optimization, Computers & Structures 182 (2017) 430–447.

[62] B. R. Mace, E. Manconi, Wave motion and dispersion phenomena: Veering, locking and strong coupling effects, The Journal of the Acoustical Society of America 131 (2) (2012) 1015–1028.

[63] B. R. Mace, D. Duhamel, M. J. Brennan, L. Hinke, Finite element prediction of wave motion in structural waveguides, The Journal of the Acoustical Society of America 117 (5) (2005) 2835–2843.

[64] L. Brillouin, Wave propagation in periodic structures: electric filters and crystal lattices.

[65] F. Maurin, C. Claeys, E. Deckers, W. Desmet, Probability that a band-gap extremum is located on the irreducible brillouin-zone contour for the 17 different plane crystallographic lattices, International Journal of Solids and Structures 135 (2018) 26–36.

[66] A. Aît-Mokhtar, R. Belarbi, F. Benboudjema, N. Burlion, B. Capra, M. Carcasses, J.-B. Colliat, F. Cussigh, F. Deby, F. Jacquemot, et al., Experimental investigation of the variability of concrete durability properties, Cement and concrete research 45 (2013) 21–36.

[67] F. Chen, Z. Jiang, J. Deng, G. Wang, D. Zhang, Q. Zhao, L. Cai, S. Q. Shi, Evaluation of the uniformity of density and mechanical properties of bamboo-bundle laminated veneer lumber (blvl), BioResources 9 (1) (2014) 554–565.

[68] J. Mueller, D. Courty, M. Spielhofer, R. Spolenak, K. Shea, Mechanical properties of interfaces in inkjet 3D printed single-and multi-material parts, 3D Printing and Additive Manufacturing 4 (4) (2017) 193–199.

[69] E. Pei, A. Lanzotti, M. Grasso, G. Staiano, M. Martorelli, The impact of process parameters on mechanical properties of parts fabricated in pla with an open-source 3-d printer, Rapid Prototyping Journal (2015).

[70] W. E. Luecke, J. A. Slotwinski, Mechanical properties of austenitic stainless steel made by additive manufacturing, Journal of research of the National Institute of Standards and Technology 119 (2014) 398.

[71] E. S. De Cursi, R. Sampaio, Uncertainty quantification and stochastic modeling with matlab, Elsevier, 2015.

[72] C.-C. Li, A. Der Kiureghian, Optimal discretization of random fields, Journal of engineering mechanics 119 (6) (1993) 1136–1154.

[73] B. Sudret, A. Der Kiureghian, Stochastic finite element methods and reliability: a state-of-the-art report, Department of Civil and Environmental Engineering, University of California, 2000.

[74] A. T. Fabro, D. Beli, N. S. Ferguson, J. R. F. Arruda, B. R. Mace, Wave and vibration analysis of elastic metamaterial and phononic crystal beams with slowly varying properties, Wave Motion 103 (2021) 102728.

[75] V. F. Dal Poggetto, J. R. F. Arruda, Widening wave band gaps of periodic plates via shape optimization using spatial Fourier coefficients, Mechanical Systems and Signal Processing 147 (2021) 107098.

[76] V. D. Lima, L. G. G. Villani, J. F. Camino, J. R. F. Arruda, Band gap optimization of one-dimension elastic waveguides using spatial Fourier plane wave expansion coefficients, Proceedings of the Institution of Mechanical Engineers, Part C: Journal of Mechanical Engineering Science (2021) 1–15.

[77] R. W. Shonkwiler, F. Mendivil, Explorations in Monte Carlo Methods, Springer Science & Business Media, 2009.

[78] R. Y. Rubinstein, D. P. Kroese, Simulation and the Monte Carlo method, Vol. 10, John Wiley & Sons, 2016.

[79] T. R. Tauchert, Energy principles in structural mechanics, McGraw-Hill Companies, 1974.

[80] S. S. Rao, Vibration of continuous systems, 2nd Edition, Wiley Online Library, 2019.

[81] T. A. Black, Spectral element analysis of bars, beams, and levy plates, Ph.D. thesis, Virginia Tech (2005).

[82] J. Hutchinson, Shear coefficients for timoshenko beam theory, J. Appl. Mech. 68 (1) (2001) 87–92.

[83] U. Lee, Spectral element method in structural dynamics, Wiley Online Library, 2009.

[84] D. Beli, J. R. F. Arruda, Influence of additive manufacturing variability in elastic band gaps of beams with periodically distributed resonators, in: Proceedings of the 3rd International Symposium on Uncertainty Quantification and Stochastic Modeling, 2016.

[85] A. Y.-T. Leung, An accurate method of dynamic condensation in structural analysis, International Journal for Numerical Methods in Engineering 12 (11) (1978) 1705–1715.

[86] R. J. Guyan, Reduction of stiffness and mass matrices, American Institute of Aeronautics and Astronautics' Journal 3 (2) (1965) 380–380.

[87] S. Gopalakrishnan, J. Doyle, Spectral super-elements for wave propagation in structures with local non-uniformities, Computer methods in applied mechanics and engineering 121 (1-4) (1995) 77–90.

[88] G. H. Golub, C. F. Van Loan, Matrix computations, 3rd Edition, North Holland, 2013.

[89] J. S. Przemieniecki, Theory of matrix structural analysis, Courier Corporation, 1985.

[90] D. Beli, J. Arruda, M. Ruzzene, Wave propagation in elastic metamaterial beams and plates with interconnected resonators, International Journal of Solids and Structures 139 (2018) 105–120.

[91] E. Bodewig, Matrix calculus, Vol. 2, North-Holland Publishing Co, 1956.

[92] E. Manconi, S. Sorokin, R. Garziera, A. Soe-Knudsen, Wave motion and stop-bands in pipes with helical characteristics using wave finite element analysis, Journal of Applied and Computational Mechanics 4 (Special Issue: Applied and Computational Issues in Structural Engineering) (2018) 420–428.

[93] S. Sorokin, E. Manconi, L. Ledet, R. Garziera, Wave propagation in helically orthotropic elastic cylindrical shells and lattices, International Journal of Solids and Structures 170 (2019) 11–21.

[94] S. K. Awasthi, U. Malaviya, S. P. Ojha, N. K. Mishra, B. Singh, Design of a tunable polarizer using a one–dimensional nano sized photonic bandgap structure, Progress In Electromagnetics Research 5 (2008) 133–152.

[95] E. Manconi, S. Sorokin, R. Garziera, Wave propagation in pipes with helical patterns, in: 6th ECCOMAS Thematic Conference on Computational Methods in Structural Dynamics and Earthquake.

[96] C. Robert, Machine learning, a probabilistic perspective, Taylor & Francis, 2014.

[97] D. C. Montgomery, E. A. Peck, G. G. Vining, Introduction to linear regression analysis, Vol. 821, John Wiley & Sons, 2012.

Appendix A. Spectral element method

Using the strain, kinetic, and potential energy, and Hamilton's principle, it is possible to obtain the equations of motion for the elementary rod, EB and T beam [79, 80, 53, 81, 82, 60]

$$\frac{\partial}{\partial x}\left(EA\frac{\partial u_x}{\partial x}\right) - \rho A\frac{\partial^2 u_x}{\partial t^2} = q_n(x,t); \tag{A.1}$$

$$\frac{\partial^2}{\partial x^2}\left(EI\frac{\partial^2 u_y}{\partial x^2}\right) + \rho A\frac{\partial^2 u_y}{\partial t^2} = q_y(x,t) \tag{A.2}$$

$$\begin{aligned} GA\kappa\left(\frac{\partial^2 v_y}{\partial x^2} - \frac{\partial \phi_z}{\partial x}\right) - \rho A\frac{\partial^2 v_y}{\partial t^2} = q_v(x,t), \\ \frac{\partial}{\partial x}\left(EI\frac{\partial \phi_z}{\partial x}\right) + GA\kappa\left(\frac{\partial v_y}{\partial x} - \phi_z\right) - \rho I\frac{\partial^2 \phi_z}{\partial t^2} = q_m(x,t), \end{aligned} \tag{A.3}$$

where the mechanical properties E, ρ, and G are, respectively, the material Young's modulus, mass density, and shear modulus. The geometric properties A, I, and κ are, respectively, the element cross-sectional area, second moment of area, and T shear coefficient. The quantities u_x, v_y, ϕ_z, $q_n(x,t)$, $q_y(x,t)$, $q_v(x,t)$, and $q_m(x,t)$ are, respectively, the element longitudinal and transversal (the EB and T) displacements, T beam shear deformation angle, and the rod and beam (transverse and rotational) external loads.

Transforming Eqs. (A.1) and (A.3) from the time to the frequency domain (Fourier series or integral, depending on the type of excitation) yields an ordinary differential equation in the spatial variable x. Substituting an exponential solution, the analytical wavenumber for each frequency ω for an homogeneous element (we have used the sub-indices $\square_r$ for rod, $\square_{eb}$ for EB beam, $\square_{tb}$ for T beam) can be obtained [6, 53, 83]

$$k_r(\omega) = \omega\sqrt{\frac{\rho}{E}}, \qquad k_{eb}(\omega) = \left(\omega^2\frac{\rho A}{EI}\right)^{1/4}, \tag{A.4}$$

$$k_{tb,1} = -k_{tb,2} = \sqrt{\frac{-\bar{\beta} + \sqrt{\bar{\beta}^2 - 4\bar{\eta}}}{2}} \qquad k_{tb,3} = k_{tb,4} = \sqrt{\frac{-\bar{\beta} - \sqrt{\bar{\beta}^2 - 4\bar{\eta}}}{2}}, \tag{A.5}$$

where $\bar{\eta} = a_1\omega^2\left(\frac{a_2 * w(n)^2 - a_3}{\bar{\Delta}}\right)$, $\bar{\beta} = a_3 a_4 - \omega^2\left(\frac{a_1 + a_2 + a_2 a_4}{\bar{\Delta}}\right)$, $\bar{\Delta} = 1 + a_4$, $a_1 = \frac{\rho A}{\kappa GA}$, $a_2 = \frac{\rho I}{EI}$, $a_3 = \frac{\kappa GA}{EI}$, $a_4 = \frac{P}{\kappa GA}$.

Using the relation between forces and/or moments and displacements and/or rotations, one can find the dynamic stiffness matrix for a spectral element of length L for the rod ($\boldsymbol{D}_r(\omega)$), EB beam ($\boldsymbol{D}_{eb}(\omega)$),and T beam elements ($\boldsymbol{D}_{tb}(\omega)$).

$$\boldsymbol{D}_r(\omega) = \frac{EA}{L}\begin{bmatrix} D_{r,11} & D_{r,12} \\ D_{r,12} & D_{r,11} \end{bmatrix}, \tag{A.6}$$

$$\boldsymbol{D}_{eb}(\omega) = \frac{EI}{L^3}\begin{bmatrix} D_{eb,11} & D_{eb,12} & D_{eb,13} & D_{eb,14} \\ D_{eb,21} & D_{eb,22} & D_{eb,23} & D_{eb,24} \\ D_{eb,31} & D_{eb,32} & D_{eb,33} & D_{eb,34} \\ D_{eb,41} & D_{eb,42} & D_{eb,43} & D_{eb,44} \end{bmatrix}, \tag{A.7}$$

$$\boldsymbol{D}_{tb}(\omega) = \boldsymbol{H}_1\boldsymbol{H}_2^{-1}. \tag{A.8}$$

The elements of the rod dynamic stiffness matrix ($\mathbf{D}_r$) are given by

$$\begin{aligned} D_{r,11} &= (k_r(\omega)L)\cot(k_r(\omega)L), \\ D_{r,12} &= -(k_r(\omega)L)\csc(k_r(\omega)L). \end{aligned} \tag{A.9}$$

The elements of matrix ($\mathbf{D}_{eb}$) are given by

$$\begin{aligned} D_{eb,11} &= D_{eb,33} = \Delta B\bar{L}^3(cos(\bar{L})sinh(\bar{L}) + sin(\bar{L})cosh(\bar{L})), \\ D_{eb,22} &= D_{eb,44} = \Delta B\bar{L}^3 k_{eb}(\omega)^{-2}(-cos(\bar{L})sinh(\bar{L}) + sin(\bar{L})cosh(\bar{L})), \\ D_{eb,12} &= D_{eb,21} = -D_{eb,34} = -D_{eb,43} = \Delta B\bar{L}^3 k_{eb}(\omega)^{-1}(sin(\bar{L})sinh(\bar{L})), \\ D_{eb,13} &= D_{eb,31} = -\Delta B\bar{L}^3(sin(\bar{L}) + sinh(\bar{L})), \\ D_{eb,14} &= D_{eb,41} = -D_{eb,23} = -D_{eb,32} = \Delta B\bar{L}^3 k_{eb}(\omega)^{-1}(-cos(\bar{L}) + cosh(\bar{L})), \\ D_{eb,24} &= D_{eb,42} = \Delta B\bar{L}^3 k_{eb}(\omega)^{-2}(-sin(\bar{L}) + sinh(\bar{L})), \end{aligned} \tag{A.10}$$

where $\bar{L} = k_{eb}(\omega)L$ and $\Delta B = \frac{1}{1-cos(\bar{L})cosh(\bar{L})}$. The matrices that compound the beam dynamic stiffness matrix ($\mathbf{D}_{tb}$) are

$$\boldsymbol{H}_2 = \begin{bmatrix} 1 & 1 & 1 & 1 \\ \varepsilon_1 & \varepsilon_2 & \varepsilon_3 & \varepsilon_4 \\ e_1 & e_2 & e_3 & e_4 \\ e_1\varepsilon_1 & e_2\varepsilon_2 & e_3\varepsilon_3 & e_4\varepsilon_4 \end{bmatrix} \tag{A.11}$$

$$\boldsymbol{H}_1 = \frac{EI}{L^3}\begin{bmatrix} -g_1 & -g_2 & -g_3 & -g_4 \\ -h_1 & -h_2 & -h_3 & -h_4 \\ e_1 g_1 & e_2 g_2 & e_3 g_3 & e_4 g_4 \\ e_1 h_1 & e_2 h_2 & e_3 h_3 & e_4 h_4 \end{bmatrix}, \tag{A.12}$$

where $\varepsilon_i = \frac{ia_3 k_i}{(k_i^2 - (a_2\omega^2 - a_3))}$, $e_i = e^{ik_i L}$, $g_i = ia_3((1 + a4)k_i + i\varepsilon_i)$, $h_i = ik_i\varepsilon_i$.

Due to reciprocity, spectral element matrices are symmetric. The dynamic stiffness matrix relates forces and displacements at the ends of the element in the frequency domain [84]:

$$\begin{Bmatrix} \boldsymbol{F}(0) \\ \boldsymbol{F}(L) \end{Bmatrix} = \begin{bmatrix} \boldsymbol{D}_{11} & \boldsymbol{D}_{12} \\ \boldsymbol{D}_{21} & \boldsymbol{D}_{22} \end{bmatrix} \begin{Bmatrix} \boldsymbol{q}(0) \\ \boldsymbol{q}(L) \end{Bmatrix}, \tag{A.13}$$

where $\boldsymbol{F}(0)$ and $\boldsymbol{F}(L)$ are the external forces, and $\boldsymbol{q}(0)$ and $\boldsymbol{q}(L)$ are vectors of the displacements at the boundaries of the simulated element. The presented methodology has an assumption of homogeneity of the element. If the element has spatially varying geometry of mechanical properties, it can be discretized.

Appendix B. Dynamic stiffness condensation for a frame element

The SEM assumes homogeneity of element properties along each element. For an element with properties varying along x according to $f(x)$, the property can be discretized with intervals $\delta x'_n$ with a zero-order approximation. For a discretized frame element (1b), matrix $\boldsymbol{D}(\omega)$ has n internal DOFs or $n+1$ segments, partitioned in internal (I) DOFs, besides left (L) and right (R) external node DOF. The internal DOF can be related to the local coordinate system (x'), separated by distances $\delta x'_i$ as shown in Fig. B.1.

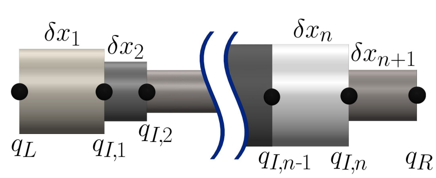

Figure B.1: Schematic representation of one-dimensional internal and external nodes of a frame element with arbitrary geometry.

Assuming there are no external forces applied to the internal nodes ($\mathbf{F}_\mathrm{I} = \mathbf{0}$), $\boldsymbol{D}(\omega)$ can be dynamically condensed. A possible procedure is to reorganize Eq. (2) by partitioning matrix $\boldsymbol{D}(\omega)$ and vector $\mathbf{q}$ as

$$\begin{bmatrix} \begin{bmatrix} \boldsymbol{D}_\mathrm{LL} & \boldsymbol{D}_\mathrm{LR} \\ \boldsymbol{D}_\mathrm{RL} & \boldsymbol{D}_\mathrm{RR} \end{bmatrix} & \begin{bmatrix} \boldsymbol{D}_\mathrm{LI} \\ \boldsymbol{D}_\mathrm{RI} \end{bmatrix} \\ \begin{bmatrix} \boldsymbol{D}_\mathrm{IL} & \boldsymbol{D}_\mathrm{IR} \end{bmatrix} & \begin{bmatrix} \boldsymbol{D}_\mathrm{ss,II} \end{bmatrix} \end{bmatrix} \begin{Bmatrix} \mathbf{q}_\mathrm{L} \\ \mathbf{q}_\mathrm{R} \\ \mathbf{q}_\mathrm{I} \end{Bmatrix} = \begin{Bmatrix} \mathbf{F}_\mathrm{L} \\ \mathbf{F}_\mathrm{R} \\ \mathbf{0} \end{Bmatrix}, \tag{B.1}$$

with

$$\boldsymbol{D}_\mathrm{aa} = \begin{bmatrix} \boldsymbol{D}_{LL} & \boldsymbol{D}_\mathrm{LR} \\ \boldsymbol{D}_\mathrm{RL} & \boldsymbol{D}_\mathrm{RR} \end{bmatrix}, \boldsymbol{D}_\mathrm{as} = \begin{bmatrix} \boldsymbol{D}_\mathrm{LI} \\ \boldsymbol{D}_\mathrm{RI} \end{bmatrix}, \boldsymbol{D}_\mathrm{sa} = \begin{bmatrix} \boldsymbol{D}_\mathrm{IL} & \boldsymbol{D}_\mathrm{IR} \end{bmatrix}, \text{ and } \quad \boldsymbol{D}_\mathrm{ss} = \begin{bmatrix} \boldsymbol{D}_\mathrm{II} \end{bmatrix} \tag{B.2}$$

where the subscripts a and s represent, respectively, active (L and R) and slave (I) DOFs [85]. Then, through applying the dynamic reduction [85], which is similar to the Guyan reduction [86], but considering the dynamic stiffness matrix (which also takes inertia into account), to $\boldsymbol{D}(\omega)$ the condensed dynamic stiffness matrix ($\boldsymbol{D}_c(\omega)$) expressed in Eq. (B.3) is obtained from Eq. (B.1) [87]

$$\boldsymbol{D}_c(\omega) = \boldsymbol{D}_\mathrm{aa} - \boldsymbol{D}_\mathrm{as}\boldsymbol{D}_\mathrm{ss}^{-1}\boldsymbol{D}_\mathrm{sa} = \begin{bmatrix} \boldsymbol{D}_\mathrm{c,LL} & \boldsymbol{D}_\mathrm{c,LR} \\ \boldsymbol{D}_\mathrm{c,RL} & \boldsymbol{D}_\mathrm{c,RR} \end{bmatrix}. \tag{B.3}$$

The matrix relation considering $\boldsymbol{D}_\mathrm{c}(\omega)$ can be written to relate quantities at nodes L and R as

$$\begin{bmatrix} \boldsymbol{D}_\mathrm{c,LL} & \boldsymbol{D}_\mathrm{c,LR} \\ \boldsymbol{D}_\mathrm{c,RL} & \boldsymbol{D}_\mathrm{c,RR} \end{bmatrix} \begin{Bmatrix} \mathbf{q}_\mathrm{L} \\ \mathbf{q}_\mathrm{R} \end{Bmatrix} = \begin{Bmatrix} \mathbf{F}_\mathrm{L} \\ \mathbf{F}_\mathrm{R} \end{Bmatrix}. \tag{B.4}$$

Appendix C. Dynamic stiffness condensation for the proposed two-dimensional frame cell

The current Appendix is also used to model the frames that are assembled into the two-dimensional frame cell that is to calculate the wavenumber values. The dynamic stiffness matrix for the proposed two-dimensional frame cell (Fig.

1a) can be assembled maintaining the nodes 4 and 5 in the last rows and columns

$$\boldsymbol{D}(\omega) = \begin{bmatrix} \begin{bmatrix} \boldsymbol{D}^*_{II,1} & \mathbf{0} & \mathbf{0} \\ \mathbf{0} & \boldsymbol{D}^*_{11,2} & \mathbf{0} \\ \mathbf{0} & \mathbf{0} & \boldsymbol{D}^*_{11,4} \end{bmatrix} & \begin{bmatrix} \boldsymbol{D}^*_{12,1} & \boldsymbol{D}^*_{12,3} \\ \boldsymbol{D}^*_{12,2} & \mathbf{0} \\ \mathbf{0} & \boldsymbol{D}^*_{12,4} \end{bmatrix} \\ \\ \begin{bmatrix} \boldsymbol{D}^*_{21,1} & \boldsymbol{D}^*_{21,2} & \mathbf{0} \\ \boldsymbol{D}^*_{21,3} & \mathbf{0} & \boldsymbol{D}^*_{21,4} \end{bmatrix} & \begin{bmatrix} \boldsymbol{D}^*_{II,2} & \mathbf{0} \\ \mathbf{0} & \boldsymbol{D}^*_{II,3} \end{bmatrix} \end{bmatrix} = \begin{bmatrix} \boldsymbol{D}_{aa} & \boldsymbol{D}_{as} \\ \boldsymbol{D}_{sa} & \boldsymbol{D}_{ss} \end{bmatrix}, \tag{C.1}$$

where

$$\begin{aligned} \boldsymbol{D}^*_{\mathrm{II},1} &= \boldsymbol{D}^*_{11,1} + \boldsymbol{D}^*_{11,3}, \\ \boldsymbol{D}^*_{\mathrm{II},1} &= \boldsymbol{D}^*_{11,2} + \boldsymbol{D}^*_{22,1}, \\ \boldsymbol{D}^*_{\mathrm{II},1} &= \boldsymbol{D}^*_{22,3} + \boldsymbol{D}^*_{11,4}, \end{aligned} \tag{C.2}$$

and $\boldsymbol{D}^*_{rs,j}$ is the sub-matrix in the r-th row and s-th column of the partitioned stiffness matrix of the j-th frame element.

Appendix D. Solving the eigenproblem via companion matrix

Equation (7) is a polynomial problem with roots λ_x, λ_y:

$$\begin{aligned} &[\boldsymbol{D}_{31}\lambda_x + \boldsymbol{D}_{21}\lambda_y + \boldsymbol{D}_{32}\lambda_x^2 + \boldsymbol{D}_{23}\lambda_y^2 + (\boldsymbol{D}_{11} + \boldsymbol{D}_{22} + \boldsymbol{D}_{33})\lambda_x\lambda_y + \\ &\quad \boldsymbol{D}_{12}\lambda_x^2\lambda_y + \boldsymbol{D}_{13}\lambda_x\lambda_y^2]\hat{\mathbf{q}}_1 = \mathbf{0}. \end{aligned} \tag{D.1}$$

where λ_x and λ_y represent half the periodicity of the periodic cell along the x and y directions shown in Fig. 1.

Equation (D.1) has two variables to be determined and there are two methods for solving it assuming one does not know k_y or k_x [51]. The first method solves the eigenproblem for an arbitrary θ numerically, which has an extreme computational cost. The second one assumes the decomposition of k into k_x and k_y as projections using a Cartesian coordinate system, i.e., for a given direction defined only by θ, $k_x = k\cos(\theta)$ and $k_y = k\sin(\theta)$. This allows to take λ_y in terms of λ_x

$$\lambda_x = e^{\frac{-ik_xL_x}{2}}, \qquad \lambda_y = \lambda_x^{\left(\frac{L_y}{L_x}\tan(\theta)\right)}. \tag{D.2}$$

Hence, if $\frac{L_y}{L_x}\tan(\theta)$ is an integer number, the problem is formulated using a single variable, for instance, k_x. An eigenproblem can be established to find λ_x and, consecutively, λ_y. The companion matrix [88, 89] can be used to solve this eigenproblem. However, the order of the polynomial will increase as a function of $\frac{L_y}{L_x}\tan(\theta)$, as can be noted by observing Eqs. (D.2) and (D.1). This method is much less computationally expensive than the first method, and it is more suitable for a statistical analysis that requires solving it several times.

It is possible to obtain the dispersion diagram scanning the first Brillouin zone (FBZ), represented in Fig. 4a, calculating the response for any values of θ [90]. In addition, as the metastructure made of elementary cells (Fig. 1) is symmetric with respect to the axes x and y, it is needed to scan only the IBZ to check for a complete band gap [65]. As presented in Fig. 4a, the contour of the IBZ consists of three directions: from $\mathbf{\Gamma}$ to $\mathbf{M}$, where $\theta = 45°$ and, therefore, $k_x = k_y$ and $\lambda_x = \lambda_y$; from $\mathbf{M}$ to $\mathbf{X}$, where θ varies between 45° and 90°, and, therefore, the polynomial in Eq. (D.1) can be ordinary, for instance, when θ is 63.435° ($k_y = 2k_x$),or 75.964° ($k_y = 4k_x$), and it can be also fractional [14]. From $\mathbf{X}$ to $\mathbf{\Gamma}$ ($\theta = 90°$), the wavenumbers are $k_x = 0$, which implies $\lambda_x = 1$.

Considering only the solution of the ordinary polynomial (Eq. (D.1)), as the order of the polynomial increases, the number of possible eigenvalues will also increase [91]. Moreover, this procedure can be computational costly and ill-conditioned. Hence, it is a common procedure to calculate the wavenumber values for a restricted number of values of θ in the IBZ (usually 2 or 3) [92, 93, 94, 95]. First, in the present study, in order to simplify the problem and make it computationally more efficient, ordinary polynomials were used. Therefore, the IBZ defined by the red line in Fig. 4a was scanned. Finally, values of θ were selected as 45°, 63.435°, and 75.964°, which made it possible to obtain three almost equally spaced regions observations over the IBZ contour in the $\mathbf{M} - \mathbf{X}$ direction of the IBZ (Fig. 4b). The same procedure can be applied when the k_x- and k_y-axis directions are redefined, allowing the computation of other directions of propagation, as presented in Appendix H.

Appendix E. Improving the invertibility of a matrix: considerations for implementation

If the determinant of a matrix is almost equal to zero, the numerical calculations of the inverse terms can be inaccurate. One procedure to overcome this issue is based on the Tikhonov regularization [88]. This methodology is based, similar to the generalized estimator for the ridge regression methodology [96], on adding a small quantity δ_T to the diagonal elements of the matrix before calculating its inverse. The scalar δ_T should be relatively small in order not to influence the final result, but large enough to make the matrix numerically non-singular.

A commonly used measure to verify the ill-conditioning of a matrix is the ratio between the maximum and minimum values of its eigenvalues (K_M) [97]. Considering δ_T the dependent variable, K_M of Eq. (D.1) before the addition of δ_T to its diagonal, the equation below, obtained through statistical regression [97] has been a good estimation for an initial guess of δ_T in the tested cases

$$\delta_T = e^{-22.35+0.1755\ \log(K_M)}. \tag{E.1}$$

In the present study, the defined procedure is substantively important when computing the inverse of $\boldsymbol{D}_{ss}^{-1}$ in the dynamic condensation (Eq. (B.3)) and the inverses of the required terms in the companion matrix. Appendix F presents some results to illustrate the effects of changes in the δ_T on the wavenumber values. Some modes are more robust and remain unchanged to the different values of δ_T, while other modes change too much that is possible to see it in the dispersion relation. In the current study, the robust mode that has physical meaning are called physical modes.

Two methods can be used to analyze the dispersion diagrams. The first is performed by obtaining and analyzing only the physical modes. This procedure begins with the separation of the modes, which can be performed through the difference between consecutive frequencies since the Modal Assurance Criterion behaves poorly due to the number of modes. For example, in the present case, for

$\theta = 75.964°$ the problem can result in 48 associated eigenvalues and eigenvectors. The two modes were obtained by varying the value of δ_T and keeping the two modes that remained unchanged. The second procedure consists of analyzing the attenuation of all computed modes without separating the physical modes. The second methodology is useful, again, in stochastic analyses, where values need to be easily computed many times and from which the inference can be performed. Appendix G presents a comparison between these two methods.

Appendix F. The effects of δ_T on the wavenumber values

More modes than the physical ones (physical) are calculated when the Bloch-Floquet periodic conditions are used, and the modes without physical meaning can be removed. Fig. F.1a presents the wavenumber values for $\delta_T = 0.05$ (δ_1), the value used for $\theta = 76°$ in the present study, and Fig. F.1b presents the result for $\delta_T = 0.5$ (δ_2). Some wavenumber values differ considerably such that the changes can be verified visually. Here, two values of δ_T are used, but it requires more values, usually 4 to 6, and these values should be greater than δ_1, which is calculated using Eq. E.1, in order to select those two wavenumber values.

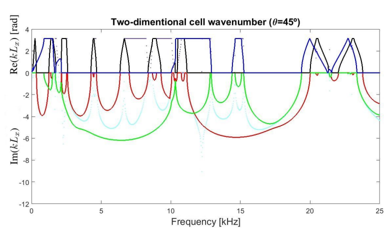

(a) Wavenumber values obtained for $\delta_1 = 0.05$ and $\theta = 45°$. physical modes, real parts in blue and black, and imaginary parts in green and red. The other modes are in cyan (imaginary parts) and purple (real parts).

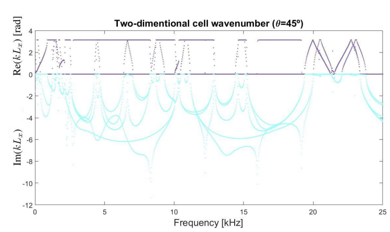

(b) Wavenumber values obtained for $\delta_2 = 10 \times \delta_1$ and $\theta = 45°$. All wavenumber values are presented in cyan (imaginary parts) and purple (real parts).

Figure F.1: Comparison between the wavenumber values for different values of δ_T for $\theta = 45°$.

The presented procedure should be performed for 6 different values of δ_T, with values of each one 10 times larger than the other begging with the value given in Eq. (E.1).

Appendix G. Comparing the full and complete band gaps obtained with different approaches

After the proposed methodology is performed, the physical wave modes are selected. Figure G.1 compares the the min|Im(k)| for the two physical wave modes in Fig. F.1a) (Fig. G.1a) with the results for all wave modes (Fig. G.1b). It is possible to notice that both results are very similar. This exemplifies that using both metrics yields the same attenuation result, but using min|Im(k)| is more efficient because it does not require to identify the physical modes, which is essential when running the stochastic response.

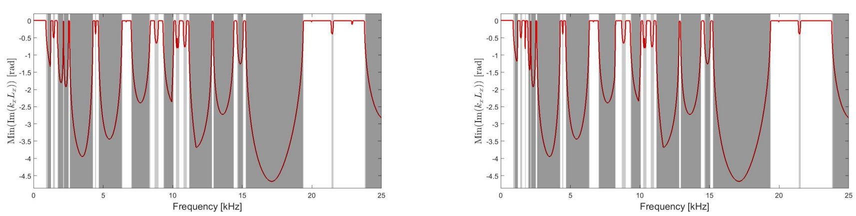

(a) Minimum of the absolute value of the wavenumber for $\theta = 45°$ when using the two physical wavemodes.

(b) Minimum of the absolute value of the imaginary part ot the wavenumber for $\theta = 45°$ when using all wavemodes.

Figure G.1: Comparison between the methodologies using the minimum of the absolute value of the imaginary part of the wavenumbers in the attenuation analysis. The gray region means attenuation for $\theta = 45°$ of at least 20% (light gray) and 60% (middle gray).

Two methods can be used to analyze the dispersion diagrams. The first is performed by obtaining and analyzing only the two wave modes that are more robust to changes in the δ_T. This procedure begins with the separation of the modes, which can be performed through the difference between consecutive frequencies since the Modal Assurance Criterion behaves poorly due to the number of modes. For example, in the present case, for $\theta \approx 76°$ the problem can result in 48 associated eigenvalues and eigenvectors. The two modes were obtained by varying the value of δ_T and keeping the two modes that remained unchanged. The second procedure consists of analyzing the attenuation for the complete and full band gap. This methodology is useful in stochastic analyses, where values need to be easily computed many times and from which the inference can be performed. Appendix F presents a comparison between the second method obtained directly from all wavenumber values and the first method using the two wave modes obtained using the first method.

Appendix H. Computing the samples along the FBZ contour

Using the same samples presented in Fig. 4b, but changing the directions of the $x-$ and $y-$axis in the physical space, as illustrated in Fig. H.1, which also alters the matrices $\mathbf{\Lambda}_L$ and $\mathbf{\Lambda}_R$ as presented in Table H.3, the the samples along the FBZ contour of the reciprocal space (k_x and k_y) can be computed. One can observe that the samples of θ varies from 0° to 360° along the FBZ contour by redefining the coordinate system, while the order of the polynomial remains the same.

Table H.3: Matrices $\mathbf{\Lambda}_L$ and $\mathbf{\Lambda}_R$ used to obtain the FBZ contour via Eq. (7).

Triangle Number	$\mathbf{\Lambda}_R^T$	$\mathbf{\Lambda}_L$	Equivalent samples of θ
1	$\begin{bmatrix} \mathbf{I}_n & \mathbf{I}_n\lambda_x & \mathbf{I}_n\lambda_y \end{bmatrix}$	$\begin{bmatrix} \mathbf{I}_n & \mathbf{I}_n\lambda_x^{-1} & \mathbf{I}_n\lambda_y^{-1} \end{bmatrix}$	45°, 63°, 76°, and 90°
2	$\begin{bmatrix} \mathbf{I}_n & \mathbf{I}_n\lambda_x^{-1} & \mathbf{I}_n\lambda_y \end{bmatrix}$	$\begin{bmatrix} \mathbf{I}_n & \mathbf{I}_n\lambda_x & \mathbf{I}_n\lambda_y^{-1} \end{bmatrix}$	104° and 117°
3	$\begin{bmatrix} \mathbf{I}_n & \mathbf{I}_n\lambda_y^{-1} & \mathbf{I}_n\lambda_x \end{bmatrix}$	$\begin{bmatrix} \mathbf{I}_n & \mathbf{I}_n\lambda_y & \mathbf{I}_n\lambda_x^{-1} \end{bmatrix}$	135°, 151°, 168°, and 180°
4	$\begin{bmatrix} \mathbf{I}_n & \mathbf{I}_n\lambda_y^{-1} & \mathbf{I}_n\lambda_x^{-1} \end{bmatrix}$	$\begin{bmatrix} \mathbf{I}_n & \mathbf{I}_n\lambda_y & \mathbf{I}_n\lambda_x \end{bmatrix}$	194° and 207°
5	$\begin{bmatrix} \mathbf{I}_n & \mathbf{I}_n\lambda_y & \mathbf{I}_n\lambda_x \end{bmatrix}$	$\begin{bmatrix} \mathbf{I}_n & \mathbf{I}_n\lambda_y^{-1} & \mathbf{I}_n\lambda_x^{-1} \end{bmatrix}$	225°, 241°, 258°, and 270°
6	$\begin{bmatrix} \mathbf{I}_n & \mathbf{I}_n\lambda_y & \mathbf{I}_n\lambda_x^{-1} \end{bmatrix}$	$\begin{bmatrix} \mathbf{I}_n & \mathbf{I}_n\lambda_y^{-1} & \mathbf{I}_n\lambda_x \end{bmatrix}$	284° and 297°
7	$\begin{bmatrix} \mathbf{I}_n & \mathbf{I}_n\lambda_x & \mathbf{I}_n\lambda_y^{-1} \end{bmatrix}$	$\begin{bmatrix} \mathbf{I}_n & \mathbf{I}_n\lambda_x^{-1} & \mathbf{I}_n\lambda_y \end{bmatrix}$	315°, 331°, 348°, and 0°
8	$\begin{bmatrix} \mathbf{I}_n & \mathbf{I}_n\lambda_x^{-1} & \mathbf{I}_n\lambda_y^{-1} \end{bmatrix}$	$\begin{bmatrix} \mathbf{I}_n & \mathbf{I}_n\lambda_x & \mathbf{I}_n\lambda_y \end{bmatrix}$	14°, and 27°

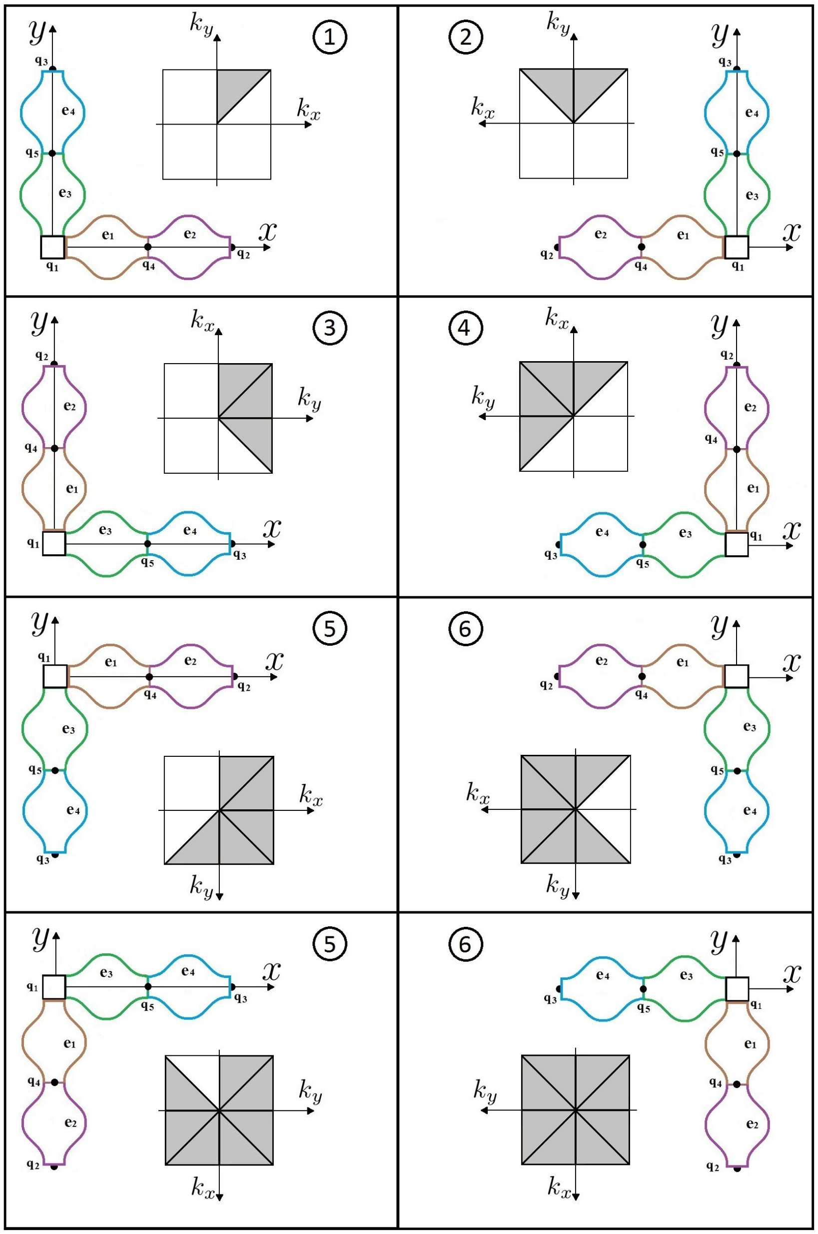

Figure H.1: Axis rotation for computing the samples along the FBZ contour.

Appendix I. Stochastic inference for the proposed direction of propagation

Figures J.1a, J.1b, J.1c, and J.1d represent the Bayes' factor (BF) with values of 3 (BF3), 10 (BF10), 30 (BF30), and 100 (BF100), as well as the median for the stochastic wavenumber, respectively, for $\theta = 90°$, $\theta \approx 76°$, $\theta \approx 63°$, and $\theta = 45°$. A large BF value indicates a large attenuation robustness computed from the deterministic two-dimensional frame cell in Fig. 2a. One can notice that, for example, the attenuation band between 15 and 20 kHz is more robust than the band gap between 11 and 13 kHz by looking to the different BF lines because it has lower spread for the proposed variability.

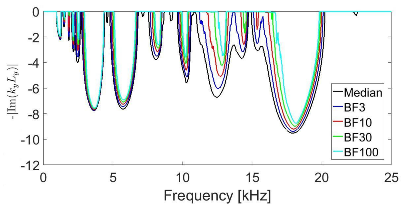

(a) **Γ-M1** direction; $\theta = 45^\circ$.

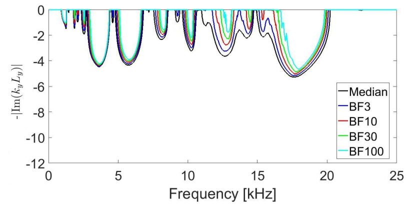

(b) One observation on the **M1-X2** direction; $\theta \approx 63^\circ$.

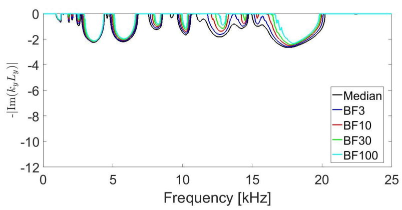

(c) One observation on the **M1-X2** direction; $\theta \approx 76^\circ$.

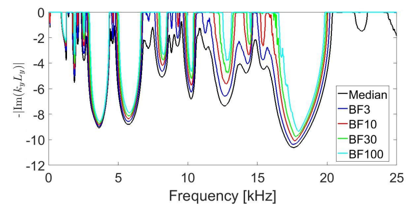

(d) **X2- Γ** direction; $\theta = 90^\circ$.

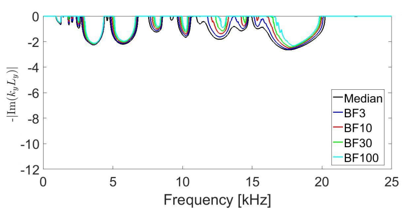

(e) One observation on the **X2-M2** direction; $\theta \approx 104^\circ$.

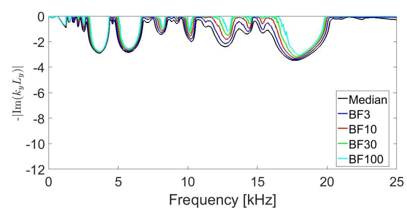

(f) **X2- M2** direction; $\theta \approx 117^\circ$.

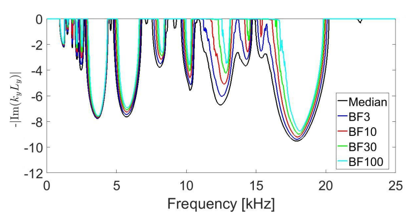

(g) One observation on the **M2**-Γ direction; $\theta = 135^\circ$.

Figure J.1: Inference using the BF to create credible intervals for the cell made of periodic plane frame elements on the stochastic wavenumber with.

Appendix J. Other stochastic results

Configuration 2 considers the variability presented in segments f_3 and f_4 of Table 2 in segments of Fig. K.1b. The inference using BF100 was used on the stochastic results of the IBZ is presented in Fig. K.2a. It is equivalent to the FBZ results presented in Fig. K.2b and Fig. K.2c, and it also agree mostly with the attenuation bands of the stochastic FRFs in Fig. K.3. As the variability is related to E and ρ for this proposed frame, there is a 4-fold rotational asymmetry between individual observation of both mechanical properties (similar to Fig. 10). However, there is 4-fold rotational symmetry between their distributions similarly as occurs for the first frame varying only E (similar to Fig. 11).

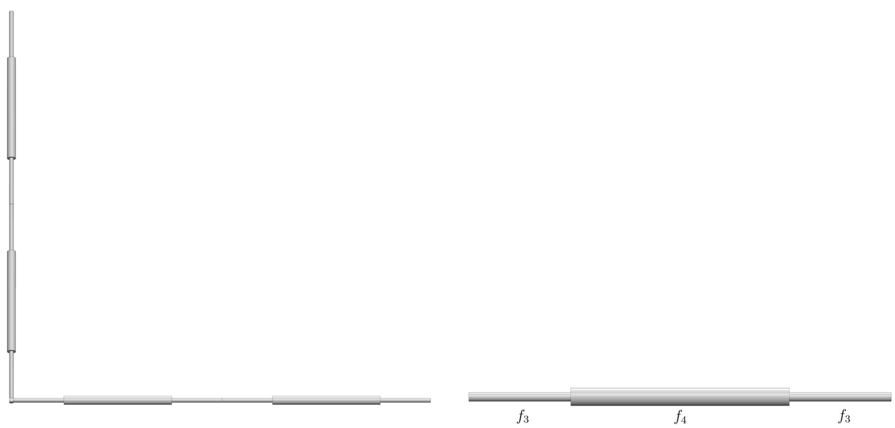

(a) (b)

Figure K.1: Another proposed unit cell made of four frame elements modeled via: (a) elementary rod and EB beam theories. The defined frame elements of nylon have: (b) two segments with a smaller cross-sectional area than the segment of the middle.

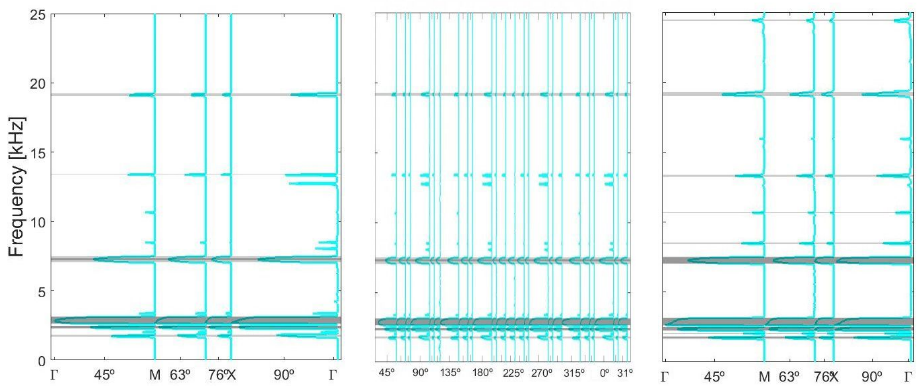

(a) (b) (c)

Figure K.2: Inference throughout the stochastic IBZ (a) and FBZ contours (b) computed using the unit cell (Fig. 1a) and the IBZ contour (c) computed using the supercell (Fig. 14), using the frame cell in Fig. K.1b. The patches represent the IBZ attenuation per cell length of at least 20% (light gray) and 60% per cell (dark gray) computed from the stochastic two-dimensional frame cell.

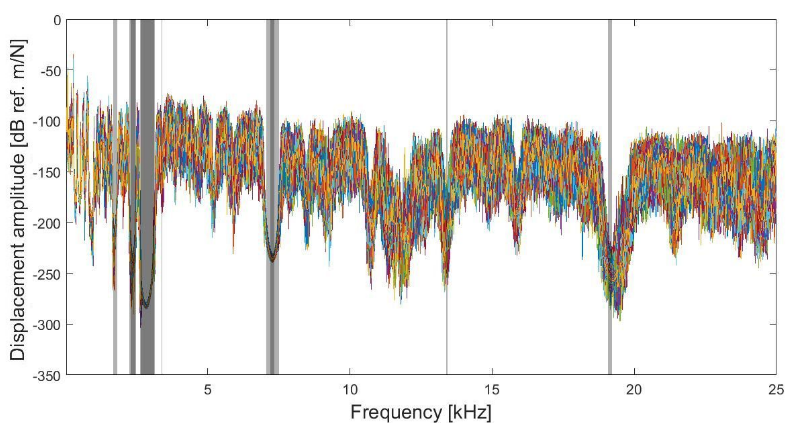

Figure K.3: Stochastic FRF, using 500 samples of the proposed metastructure (Fig. 6, vertical excitation and vertical response) made of 16 two-dimensional frame cells (Fig. K.1b) with the inference on the stochastic IBZ of a single unit cell. The patches represent the IBZ attenuation per cell length of at least 20% (light gray) and 60% per cell (dark gray) computed from the stochastic two-dimensional frame cell (Fig. K.2a).

Appendix K. Supercell analysis

A similar approach as presented in Appendix C can be applied to condensate the internal nodes of the proposed supercell (Fig. 14). Thus, considering the 3 external red nodes in Fig. 14, the terms $\mathbf{\Lambda}_R$ and $\mathbf{\Lambda}_L$ are redefined by Eq. L.1, and after $\mathbf{u}$ in Eq. 2 is replaced by $\mathbf{\Lambda}_R u_1$, and premultiplied both sides by $\mathbf{\Lambda}_L$, Eq. 7 is again obtained, but the order of the resulting polynomial is greater than the one using the two-dimensional unit cell.

$$\mathbf{\Lambda}_R = \begin{bmatrix} \mathbf{I}_n & \mathbf{I}_n\lambda_x^3 & \mathbf{I}_n\lambda_y^3 \end{bmatrix}, \mathbf{\Lambda}_L = \begin{bmatrix} \mathbf{I}_n & \mathbf{I}_n\lambda_x^{-3} & \mathbf{I}_n\lambda_y^{-3} \end{bmatrix}. \tag{L.1}$$